A fluorogenic pseudo-infection assay to probe transfer and distribution of influenza viral contents to target vesicles

Ahanjit Bhattacharya,[1,2] Nahal Bagheri,[3] Steven G. Boxer[1,*]

[1]Department of Chemistry, Stanford University, Stanford, CA-94305

[2]Stanford Center for Innovation in Global Health, Stanford University, Stanford, CA-94305

[3]Department of Electrical Engineering, Stanford University, Stanford, CA-94305

*Correspondence to: sboxer@stanford.edu

Abstract: Fusion of enveloped viruses with endosomal membranes and subsequent release of viral genome into the cytoplasm is crucial to the viral infection cycle. It is often modelled by carrying out fusion between virus particles and target lipid vesicles. We utilized fluorescence microscopy to characterize the kinetic and spatial aspects of the transfer of influenza viral ribonucleoprotein (vRNP) complexes to target vesicles and their distribution within the fused volumes to gain deeper insight into the mechanistic aspects of endosomal escape. The fluorogenic RNA-binding dye QuantiFluor® (Promega) was found to be well-suited for direct and sensitive microscopic observation of vRNPs which facilitated background-free detection and kinetic analysis of fusion events on a single particle level. To determine the extent to which the viral contents are transferred to the target vesicles through the fusion pore, we carried out virus-vesicle fusion in a side-by-side fashion. Measurement of the Euclidean distances between the centroids of super-localized membrane and content dye signals within the fused volumes allowed determination of any symmetry (or the lack thereof) between them as expected in the event of transfer (or the lack thereof) of vRNPs, respectively. We found that in case of fusion between viruses and 100 nm target vesicles, ~39% of the events led to transfer of viral contents to the target vesicles. This methodology provides a rapid, generic and cell-free method to assess the inhibitory effects of anti-viral drugs and therapeutics on the endosomal escape behavior of enveloped viruses.

Significance

Many enveloped viruses like influenza infect cells by transferring their genome to the cytoplasm upon fusing with endosomal membranes. Viral vector-based carriers and lipid nanoparticles deliver cargo to the cytoplasm through similar mechanisms. Fusion behavior of lipid vesicles with enveloped viruses and related lipid-based systems are often studied to derive mechanistic insight into the process and its outcomes. Here we present a methodology to probe the transfer of viral contents to target vesicles and its distribution within the fused volume. Our method can be applicable for quantifying the efficacies of anti-viral drugs which inhibit endosomal escape and for optimizing the efficiencies of cytoplasmic cargo delivery by nanocarriers.

Introduction

There is a long-standing interest in studying viral fusion from a biophysical perspective to dissect the underlying interplay between proteins and lipids involved in the process (1, 2). In a bottom-up biophysical model, one can precisely control the composition of the system to ascertain which components are essential to a process and quantify their molecular contributions. Fusion of virus particles with lipid vesicles, sometimes referred to as pseudo-infection, is a commonly described model of viral cellular entry under controlled conditions (pH, temperature, time, target membrane composition and curvature) (3, 4). Since viral membrane fusion is an inherently heterogeneous process, observation of a large number of such events on a single particle level can reveal pathways and mechanistic details that may remain obscure in ensemble studies (5). Until now, diffraction-limited fluorescence microscopy and cryogenic transmission electron microscopy (cryo-TEM) have been the preferred methods for studying viral fusion on a single-particle level (3). While fluorescence microscopy provides information on fusion kinetics, cryo-EM provides a direct visualization of the fusion intermediates over a population.

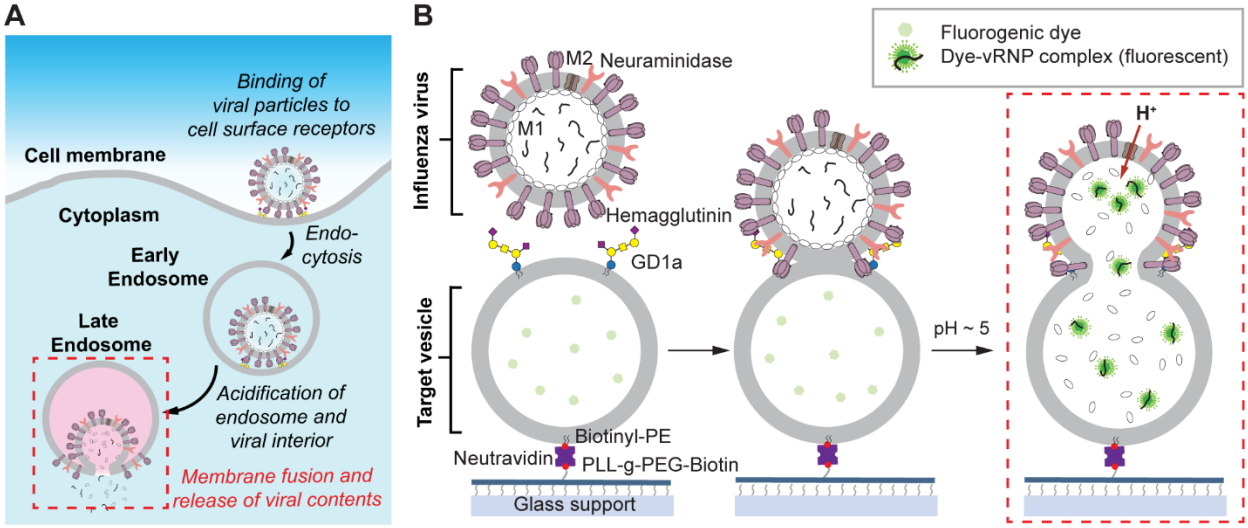

Figure 1. Pseudo-infection model of viral cellular entry. **A**. Schematic representation of the steps leading to the cellular entry of influenza virus. Fusion of a virus particle with endosomal membrane is triggered by acidification of endosomes (marked in a dashed rectangular box). **B**. Schematic representation of fusion of influenza virus particles with target vesicles tethered to a passivated and functionalized glass surface (pseudo-infection). The target vesicles encapsulate a fluorogenic nucleic acid-binding dye. In the first step, the virus particles bind to the target vesicles via sialic acid-containing lipid (GD1a) receptors (two molecules shown for simplicity). Fusion between virus particles and vesicles is triggered by a drop in pH. Upon opening of the fusion pore, the nucleic acid-binding dye molecules come in contact with the viral ribonucleoprotein (vRNP) complexes and turn on in fluorescence. This step is marked with a dashed rectangular box to highlight the analogy with endosomal membrane fusion depicted in part A.

Influenza virus is a widely studied pathogen as the causative agent of seasonal epidemics and occasional but unpredictable pandemics. It is a canonical enveloped virus which delivers its macromolecular contents to the host cell via membrane fusion (6). The lipid envelope of the influenza virions are decorated with hundreds of copies of the glycoprotein hemagglutinin (HA) which is necessary for attachment of the virions to cell surface sialic acid receptors (Figure 1A) (7). The influenza viral genome consists of eight single-stranded, negative sense RNA segments organized into macromolecular assemblies called viral ribonucleoproteins (vRNPs) (8). Electron microscopy studies on vRNPs have revealed that these are double helical structures 30-120 nm in length (9). Within the vRNPs, the RNA strand is bound to the nucleoprotein (NP) scaffold by

interaction with its phosphodiester backbone such that, on average, there is 1 NP per 24 ribonucleotides (10). Inside the virions, the vRNPs associate with the matrix protein (M1) layer. Following binding to the cell surface receptors, the virions are endocytosed within endosomes. When the pH inside the endosome drops below 5.5, HA undergoes conformational change which triggers fusion between viral and endosomal membranes. Also, M2 channels pump protons to the viral interior leading to dissociation of the M1 layer from the viral membrane which in turn becomes more amenable to fusion (11). At the same time, the interaction between the M1 proteins and vRNPs weakens and the latter are released into the cytoplasm via a fusion pore – a process known as endosomal escape (Figure 1A) (12).

The pseudo-infection model recapitulates two fundamental steps of the endosomal escape process – mixing of lipid compartments and transfer of viral contents (3) (Figure 1B). While lipid mixing between virus and vesicle membranes is a rapid way to test that the viral fusion protein is functional (13), many such events are halted at the intermediate hemifused state where the outer leaflets of the two membranes merge but not the inner leaflets, and consequently, no fusion pore is formed. On the other hand, a content mixing experiment provides more information, namely, the presence of a functional fusion protein, formation of a fusion pore, and possible presence of the viral genome, though the fusion pore may not necessarily be large enough to accommodate passage of the vRNPs (viral genome).

To observe content mixing between virus and vesicle compartments, typically, a water-soluble dye is encapsulated at self-quenching concentration within the virus or target vesicle interior which turns on in fluorescence due to dilution upon fusion (14–17). These assays have been popular because content label dyes like calcein and sulforhodamine B (SRB) are relatively inexpensive (an important practical consideration since only a small fraction of dye gets encapsulated during preparation of the target vesicles). However, they suffer from a few drawbacks. First, a very high concentration (tens of mM) of the content label dye needs to be encapsulated in the target vesicle lumen. It has been shown that dyes like SRB can strongly associate with lipid membranes (18) and therefore it can be expected that such dyes may perturb the mechanical properties of the target vesicle membranes and therefore influence the fusion behavior. Second, content loss events due to vesicle bursting complicate the analysis of these assays (19). Finally, content mixing assays based on dequenching of soluble dyes have to rely on indirect evidence and do not detect the viral macromolecular content (genome) directly. Therefore, a probe which enables direct visualization of viral RNA in infectious particles without potentially perturbing the target vesicle membranes would be highly desirable.

Fluorescence In Situ Hybridization (FISH) probes have been used to detect specific viral sequences in fixed and permeabilized viral preparations (20). However, such probes are not fluorogenic and need wash steps which limits their applicability for real-time tracking studies. Molecular beacons are fluorogenic oligonucleotide probes which turn on in fluorescence upon hybridizing with target nucleic acid sequences (21). But it is not obvious whether the complementary sites on the viral RNA will be accessible to such probes since the viral RNA typically remains bound to proteins. Moreover, to encapsulate even a few (<10) copies of molecular beacons inside target vesicles (~100 nm in diameter), one needs to start with at least tens of micromolar of the probe in the hydration solution which may pose practical challenges such as high cost. Simple nucleic acid-binding fluorogenic dyes may be advantageous in situations where detection of any viral nucleic acid is desirable. In this work, we systematically screened many commercially available nucleic-acid binding dyes to evaluate the feasibility of their use in microscopy-based viral content transfer experiment as illustrated in Figure 1B. The RNA-binding dye QuantiFluor offered the most optimal physico-chemical (brightness and photostability)

characteristics for this experiment. Using fluorescence microscopy, we probed the kinetic aspects of virus-vesicle fusion events on a single particle level. Using super-localization microscopy and a novel fusion geometry introduced below, we probed the pattern of distribution of viral contents within the fused volume to determine the efficiency of content transfer through the fusion pore. Taken together, we show that our method is applicable for semi-quantitative estimation of viral infectivity and efficiency of endosomal escape in a straightforward, cell-free manner.

Results and Discussion

Selection of a suitable nucleic acid-binding dye for content transfer experiments. Initially we screened the dyes (Table 1, Figure S1) based on the following criteria: (i) good aqueous solubility to allow vesicle formation with sufficiently high encapsulated dye concentration; (ii) fluorescence properties not significantly altered between pH 7.5 and 5; (iii) impermeability to lipid membranes; (iv) minimal binding to lipid membranes (18); (v) efficient binding to vRNPs leading to high signal above background when bound to viral RNA; and (vi) photostability. In a typical screening experiment, we prepared unilamellar vesicles (ULVs) composed of the lipids POPC:DOPE:Cholesterol:GD1a:Biotin-DPPE:Texas Red-DHPE (37.4:20:40:2:0.5:0.1 by molar ratio) and encapsulated each dye by extrusion through polycarbonate membrane filters of 100 nm pore size followed by size exclusion chromatography. The vesicles were found to have a narrow size dispersity (polydispersity index = 0.061) from dynamic light scattering (DLS) measurements (Figure S2A). Cryo-TEM imaging of the vesicles revealed that they are overwhelmingly unilamellar (Figure S2B). We targeted a bulk concentration of 10-100 µM for a given dye to ensure encapsulation of tens of molecules in a single vesicle. For all viral fusion experiments, we used simple microfluidic flow cells prepared by plasma-bonding polydimethylsiloxane (PDMS) blocks to clean glass cover slips and connecting them to a syringe pump for flowing various solutions (Figure S3). We passivated the glass surface of the flow cell with block copolymers PLL-g-PEG/PLL-g-PEG-biotin to prevent any non-specific binding of vesicles and/or virus particles (19) and attached the vesicles encapsulating a particular dye via interaction with NeutrAvidin (Figure 1B). Unbound vesicles were removed by washing with a pH 7.4 buffer (*vesicle buffer*). Next, H3N2 influenza virus particles (strain X-31, A/Aichi/68) were added to the same flow cell and allowed to incubate for about 10 min. Excess virus particles were removed by washing, and then the pH was rapidly dropped by flowing in pH 5.1 buffer (*fusion buffer*). Simultaneous with the pH drop, a continuous video stream of the slide was acquired. Bright spots were generated against minimal background if a dye bound to vRNPs (Figure 2A).

Among all dyes tested, we observed that the RNA-specific dye QuantiFluor (Promega) offered the best combination of properties necessary for detection of viral contents (Figure S4). We further tested the binding of QuantiFluor with vRNPs present in a detergent-lysed virus sample and found that the fluorescence of QuantiFluor was significantly turned on in the viral lysate (Figure 2B). The fluorescence was practically unchanged when the lysate was digested with proteinase K suggesting that NPs do not hinder binding of QuantiFluor to the viral RNA. A few members of the SYBR family of dyes also showed fluorescence turn on in the microscopy assay but they presented some limitations. The signals from SYBR Green I and SYBR Green II diminished rapidly under the standard imaging conditions due to photobleaching (Figure S5). The signal from SYBR Gold was relatively stable; however, the level of signal above background was significantly weaker as compared to QuantiFluor (Figure S5). SYBR Safe, a dye used in gel staining, did not lead to any fluorescence turn on. We tested the dye EvaGreen, a bis-intercalating dimeric acridine orange dye which is commonly used to detect dsDNA but were unable to detect any fluorescence from the microscopy experiments. We tested the performance of the dye in viral lysates and found

that when the lysate is digested with proteinase K, a much larger turn-on is observed (Figure S6). This result suggests that EvaGreen cannot bind sufficiently to the viral RNA complexed with proteins. We found that another bis-intercalating dye DiYO-1 was suitable for content transfer assay, consistent with the results described previously in an influenza viral genome exposure assay (17, 22). We further observed that DiYO-1 produced a stable signal under our imaging conditions (Figure S5), albeit we had to use a starting dye concentration of 100 µM to encapsulate sufficient dye molecules inside target vesicles to achieve appreciable signal levels as compared to 10 µM described by the previous authors. The SYTO (11-14, 16, 21, 24, 25) family of dyes was found to be completely unsuitable for content transfer experiments. Most of these dyes tended to form aggregates during vesicle preparation due to apparent hydrophobicity, and we were unable to detect any turn-on behavior in the microscopy experiments.

Table 1: Summary of the fluorogenic nucleic acid-binding dyes tested in this study.

Dye	Supplier	MW (g mol^{-1})	λ_{em} (nm)	λ_{ex} (nm)	ε_{max} ($M^{-1}cm^{-1}$)	Content transfer assay
QuantiFluor®	Promega	582.2[a]	492	540	N.A	Yes
Thiazole Green (SYBR® Green I)	Biotium	509.73	498	522	58,000	Yes
SYBR™ Green II	Thermo Fisher	454.19	497	520	--	Yes
SYBR™ Safe	Thermo Fisher	504.66	502	530	--	No
Oxazole Gold (SYBR® Gold)	Biotium	495.66	496	539	57,000	Yes
EvaGreen®	Biotium	1119.06	500	530	35,000[c]	Yes
SYTO™ 11		~400	508/510	527/530		No
SYTO™ 12		~300	499/500	519/522		No
SYTO™ 13		~400	488/491	509/514		No
SYTO™ 14	Thermo Fisher[b]	~500	517/521	549/547	>50,000	No
SYTO™ 16		~450	488/494	518/525		No
SYTO™ 21		~500	494	517		No
SYTO™ 24		~550	490	515		No
SYTO™ 25		~450	521	556		No
DiYO™-1	AAT Bioquest	1270.65	491	508	98,900	Yes
ThT-NE	Sigma Aldrich	346.92	461	495	19,000[c]	No
Qubit™ RNA BR Reagent	Thermo Fisher	N.A.	644	673	N.A	No
Indolizine dye	(synthesized)[d]	362.21	556	608	27,500	No

[a] molecular ion peak detected by MS (Figure S4C); [b] sampler kit; [c] free dye in PBS, N.A. Not available. In the case of SYTO™ 11-16, the excitation/emission wavelengths correspond to dye bound to DNA/RNA; [d] reference 24. "Yes" and "No" in the extreme right column denotes whether a particular dye is suitable for content transfer experiment or not.

We next tested a thioflavin T-derived dye ThT-NE which was previously described to bind to secondary structures of viral RNA inside cells (23). However, no fluorescence turn on was observed with the microscopy-based viral fusion assay with ThT-NE. Finally, we tested a recently developed fluorogenic indolizine dye which was described to emit red fluorescence upon binding to cellular RNA (24); however, we found that no fluorescence turn on was observed when we carried out a viral fusion assay (Figure S7A). We were unable to observe any appreciable fluorescence enhancement above background in viral lysates as well even after proteinase K

treatment (Figure S7B). In the subsequent experiments described in this paper, we used QuantiFluor as the sole content transfer dye. Unfortunately, the structure and concentration of QuantiFluor is not provided by the supplier, so we made a crude analysis to approximately determine a concentration of the working stock solution (Materials and Methods and Figure S4).

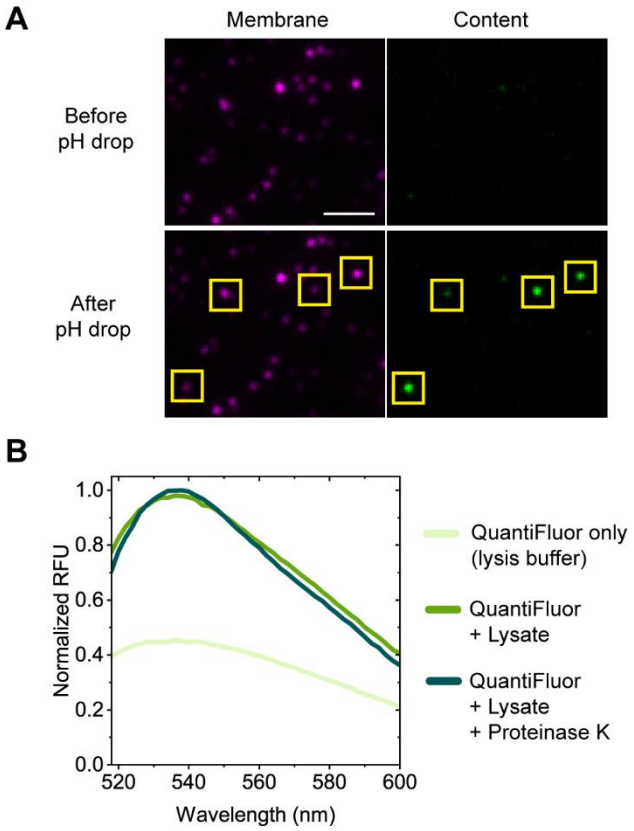

Figure 2. Screening of nucleic-acid binding dyes capable of binding to viral ribonucleoprotein (vRNP) complexes. **A**. In a typical screening experiment using the configuration shown in Figure 1B, vesicles stained with Texas Red-DHPE and encapsulating a nucleic acid-binding dye were imaged by excitation with 561 nm (membrane: *magenta*) and 488 nm (content: *green*) light before and after pH drop (i.e., 7.4 → 5.1). Appearance of a new green spot co-localizing with a magenta spot (marked in yellow squares) indicated that the dye was capable of binding to vRNPs upon membrane fusion. Scale bar: 3 μm. **B**. Fluorescence emission spectra of QuantiFluor added to influenza viral lysate showing significant turn on as compared to dye only (dissolved in *lysis buffer*).

Characterization of fusion of influenza virus with vesicles encapsulating QuantiFluor. First, we sought to measure the kinetics of content transfer over a population of viruses and vesicles of variable sizes. Unilamellar vesicles (100 nm or 200 nm ULVs) encapsulating QuantiFluor were prepared and tethered to the surface of microfluidic flow cells. We added the influenza virus particles and allowed the viruses to bind to the vesicles. Next, the pH was dropped to 5.1 and bright spots corresponding to fusion events were detected. The spots were followed by continuous imaging and intensity traces were extracted from those videos (Figure 3A, Figure S8). The time point (wait time) where we observed a sudden spike in intensity corresponded to the onset of the fusion event. Those wait times were then combined into cumulative distribution functions (CDF). From the CDFs, we observed that the content transfer kinetics of viruses with 100 nm was slightly faster than with 200 nm vesicles (Figure 3C). For comparison, we also carried out lipid mixing experiments between virus labeled with self-quenching concentration of Texas Red-DHPE and unlabeled 100 nm or 200 nm vesicles. In the event of fusion (or hemifusion),

Texas Red-DHPE underwent dilution and a sudden spike in fluorescence was observed in the intensity traces (Figure 3B). We calculated the waiting time between pH drop and appearance of a fluorescent spot and constructed CDFs to measure kinetics of lipid mixing (Figure 3C). In good agreement with previous results (17, 19), we found that lipid mixing took place at a more rapid rate as compared to that of content transfer.

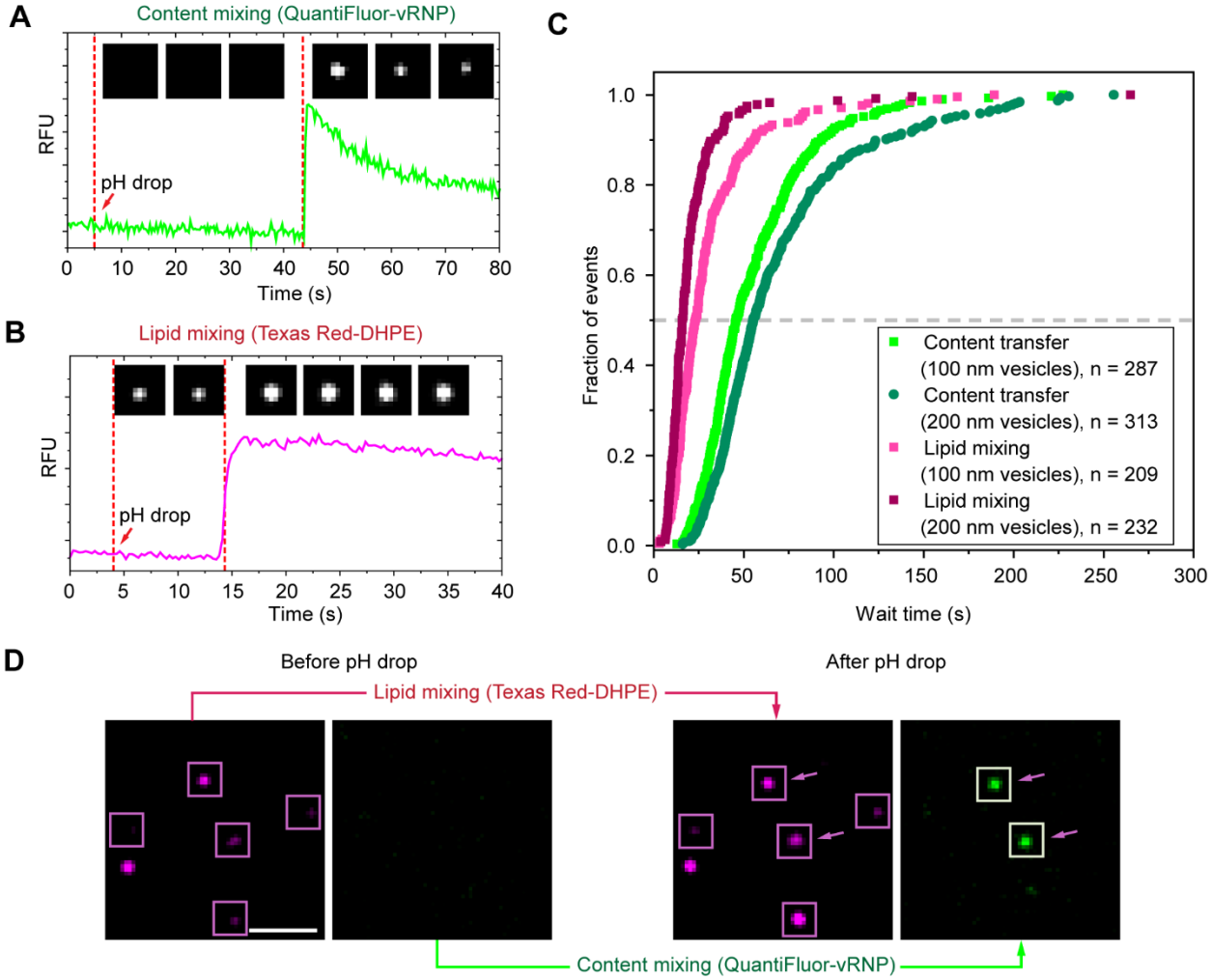

Figure 3. QuantiFluor as a fluorogenic RNA-binding dye to assay viral content transfer to target vesicles. **A**. Fluorescence intensity profile corresponding to QuantiFluor fluorescence turn on during a typical content transfer event. Micrographs corresponding to a single event are shown in inset. **B**. Fluorescence intensity profile corresponding to dequenching of Texas Red-DHPE fluorescence during a typical lipid mixing event. Micrographs corresponding to a single event are shown in inset. **C**. Cumulative distribution functions corresponding to lipid mixing and content transfer events for viral fusion with 100 nm and 200 nm vesicles. **D**. Images of 100 nm vesicles undergoing lipid mixing and content transfer (marked in square boxes). In case of a lipid mixing event, the signal in membrane channel (*magenta*) turned brighter while a new spot appeared in the content channel (*green*) due to fluorescence turn-on. The arrows indicate the virus-vesicle pairs undergoing simultaneous lipid mixing and content transfer. The events where lipid mixing took place without content transfer were likely arrested at the hemifusion stage. Scale bar: 10 µm.

Next we estimated what fraction of virus particles undergoing lipid mixing also underwent content transfer. In this experiment, the influenza virus particles were labeled with a self-quenching concentration of Texas Red-DHPE, and fusion was carried out with QuantiFluor-containing vesicles. We identified the spots which underwent an increase in fluorescence in the

Texas Red channel and also co-localized with a corresponding spot in the QuantiFluor channel (Figure 3D). We estimated that about 40% (40 out of 99) of all vesicles undergoing lipid mixing underwent content transfer. It is notable here, however, that some vesicles may have too few or no trapped dye molecules, so that when content transfer took place to those vesicles, no signal would have been detectable. So, it is possible that the actual fraction of the virus-vesicle pairs undergoing content transfer may be somewhat underestimated.

Measuring the distribution of vRNP content upon viral fusion with target vesicles. During membrane fusion, efficient release of viral contents is decided by factors such as the sizes of the fusion pores (25, 26). The vRNPs of influenza are large structures measuring tens of nm (Figure S9), so it is not obvious that they will pass through the fusion pore even though small dye molecules may. The diameter of the fusion pore has been measured using cryogenic electron tomography (cryo-ET) and is estimated to be ~15 nm at initial stages of fusion (11, 27, 28). Therefore, for transfer of vRNPs to the target vesicle, the fusion pore must expand to several tens of nanometers. Also, the vRNPs must dissociate fully from the M1 layer to freely distribute within the fused volume. Previous cryo-ET studies indeed revealed that two kinds of fused volumes may be obtained: (1) the virus and vesicle fused into a larger compartment and the viral contents were evenly distributed; (2) the virus and vesicle compartments were connected through a narrow stalk-like pore but the vRNPs were not transferred from the virus side.

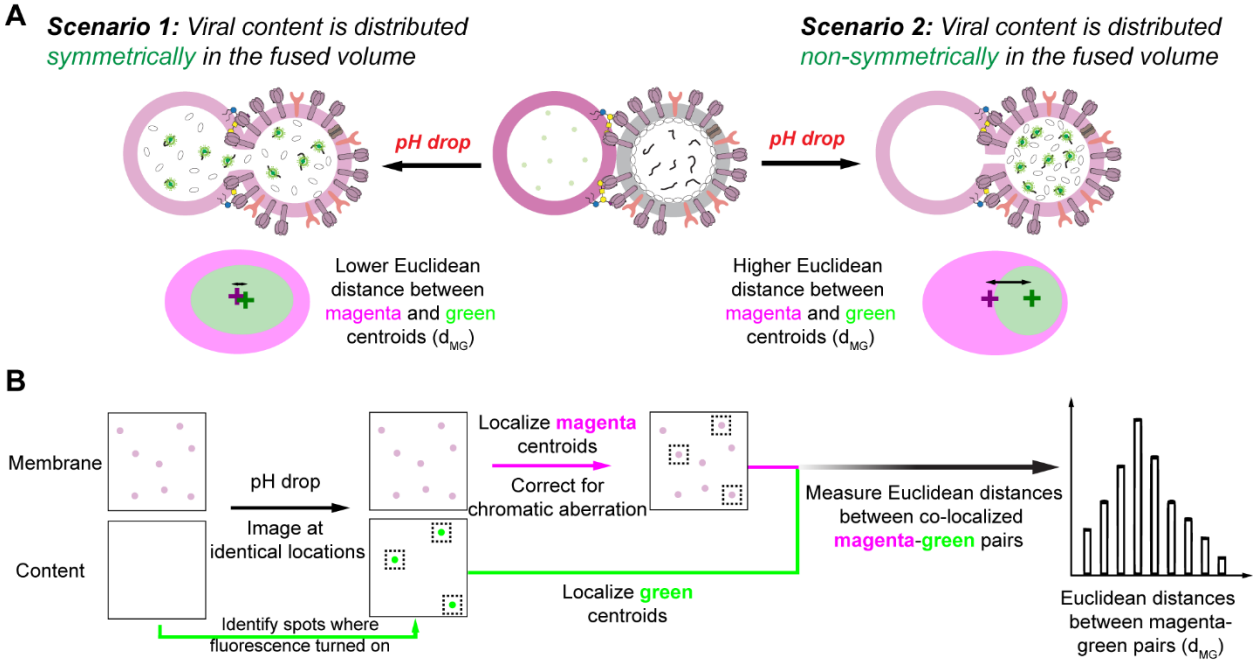

Figure 4. Schematic representation of an assay to measure the distribution of viral contents within the fusion volume. **A**. In the case where the vRNP contents are symmetrically distributed within the fusion volume, the centroids of the membrane dye (*magenta*) and content (*green*) channels overlap. Alternatively, if the viral contents are non-symmetrically distributed within the fusion volume, i.e. the QuantiFluor passed through a small fusion pore but the vRNP did not, the centroids of the membrane (*magenta*) and content (*green*) channels are spaced farther apart. **B**. Workflow of measurement of Euclidean distances between centroids of membrane (*magenta*) and content (*green*) dyes (d_{MG}) using super-localization and chromatic aberration correction procedures.

We hypothesized that super-localization microscopy techniques can be used to distinguish between the above two fusion scenarios since such techniques are widely used to pinpoint the centroid of a fluorescent particle with a lateral resolution of only a few tens of nanometers or less

(29, 30). Although both the viruses (28) and vesicles (Figure S2B) have variable morphologies and sizes, given that the dimensions of the fused volume (150-250 nm) is approximately at or below the diffraction limit, we assumed that the precise geometry of the latter will not have any significant effect on the super-localization procedure. In the case of a large fusion pore, the dye-bound fluorescent vRNPs (content) will be evenly distributed within the fused volume and the centroids of the signals from the membrane dye and the content dye should more or less overlap, therefore leading to a small Euclidean distance between them (*Scenario 1*, Figure 4A). In the case of formation of transient or small pores, the nucleic acid-binding dye (QuantiFluor), being a relatively small molecule (approximately 600 Da) (Materials and Methods), will transfer to the virus side and bind there to the vRNPs remain and turn on. The centroids of the signals from the membrane dye and the content dye should be farther apart, therefore leading to a larger Euclidean distance between them (*Scenario 2*, Figure 4A). Throughout the text and illustrations, the Euclidean distances between the centroids of the membrane (561 nm excitation, referred to as *magenta*) and content (488 nm excitation, referred to as *green*) channels are abbreviated as d_{MG}.

A schematic diagram outlining the procedure for measurement of d_{MG} values is illustrated in Figure 4B. Briefly, images are taken in *magenta* and *green* channels at various locations of the flow cell before fusion. The pH was then dropped to induce fusion and after 30 min, images were obtained in 2 channels at identical positions to identify the locations of the turned-on green spots (QuantiFluor-RNA). We needed to precisely locate the centroids of the membrane and content signals to reliably measure the distances between their centroids (Figure 4B). However, we had to address an important issue prior to carrying out distance measurements. While acquiring multichannel fluorescence images, the images acquired in different color channels are misaligned due to chromatic aberration (31). Even though advanced objective lenses correct this aberration for most practical purposes, it can still limit super-localization of diffraction-limited point sources (32). Additionally, chromatic aberration is not uniform across the field-of-view (FOV) (32). The spectral channels need to be registered to reliably interpret the extent of co-localization between signals in two channels as outlined in Figure 4B. Channel registration was accomplished by imaging multiply labeled 100 nm TetraSpeck™ beads in *magenta* (561 nm excitation) and *green* (488 nm excitation) emission channels, with the latter being the reference channel. The centroids of the point spread functions of the spots were super-localized using the FIJI plugin ThunderSTORM by 2D Gaussian fitting (33). The chromatic calibration table containing the displacement vectors across the FOV were calculated using the FIJI plugin Detection of Molecules (DoM) which uses continuous smooth B-spline grid registration (34). The coordinates of the spots in the magenta channel were corrected by vector transformation using the chromatic calibration table (Figure 5A). A distortion map generated with DoM illustrates the variability of the chromatic shift across the FOV (Figure 5B). Following this, d_{MG} values were calculated using ThunderSTORM. It was found that, in uncorrected calibration set images, d_{MG} values of approximately 0-140 nm were measured with a mean of 76.1±1.4 nm (Figure 5C). In the corrected images, d_{MG} ranged only over 0-50 nm with a mean of 8.9±0.4 nm (Figure 5C).

We next tested the performance of our distance measurement method by considering a few cases where the centers of magenta and green signals should co-localize (Figure 5D). First, we analyzed images of TetraSpeck beads separate from the images used for calibration. In the corrected images, we measured a narrow distribution of d_{MG} with a mean of 11.0±0.2 nm. Next, we calculated the d_{MG} for 50 nm, 100 nm, and 200 nm vesicles having membrane stained with Texas Red-DHPE and encapsulating Alexa Fluor 488. We obtained values of 29.2±0.5 nm, 25.7±0.8 nm and 20.7±0.7 nm respectively (Figure 5D). To test the performance with alternate green-emitting fluorescent dyes we measured d_{MG} for Texas Red-DHPE labeled 100 nm vesicles

encapsulating carboxyfluorescein and pyranine and obtained values of 28.2±0.6 nm and 28.9±0.4 nm, respectively (Figure S10).

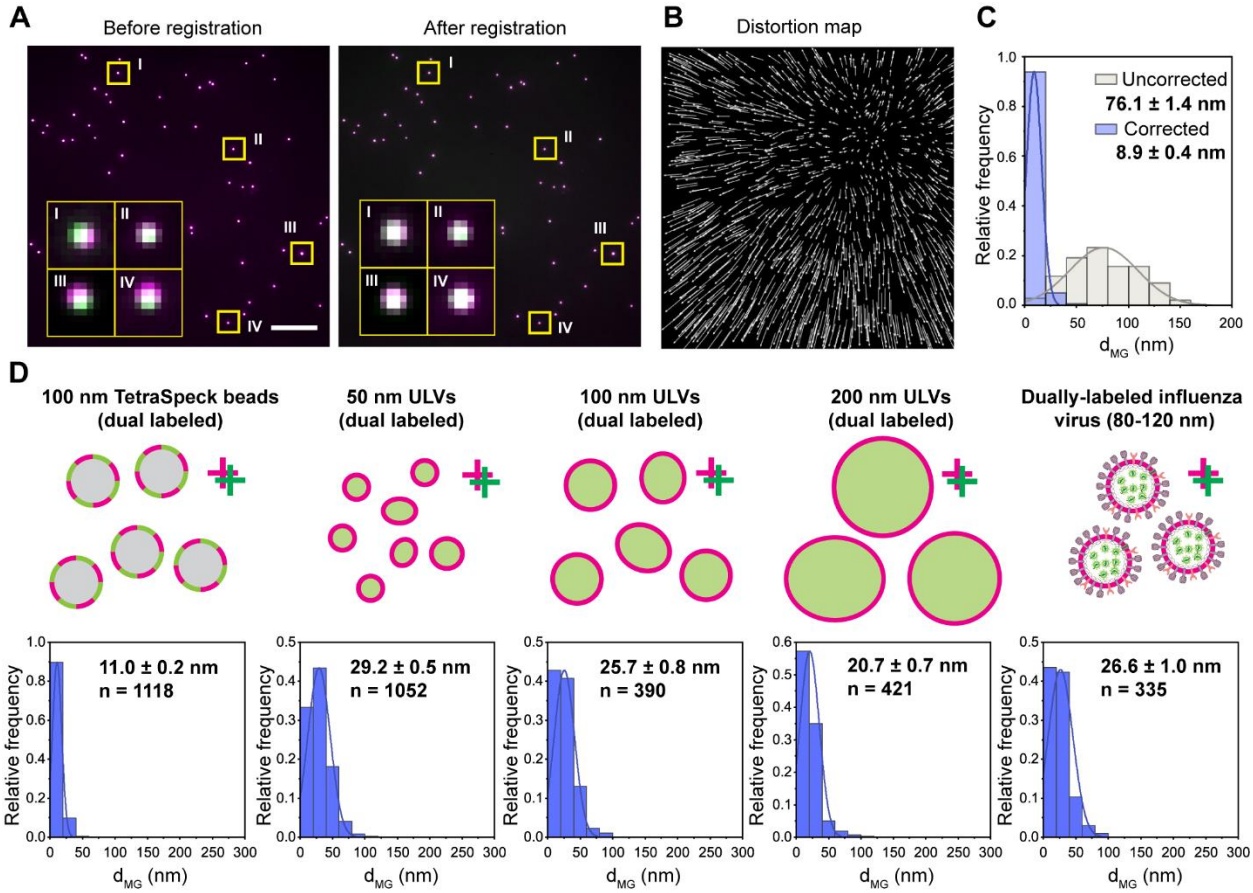

Figure 5. Measurement of Euclidean distances between the centroids of membrane and content signals. **A**. Composite of two-channel images (488 nm channel in *green* and 561 nm channel in *magenta*) of multiply labeled 100 nm TetraSpeck™ beads before (*left*) and after (*right*) registration. Images of individual beads from different parts of the field-of-view (FOV) are shown in inset. Scale bar: 20 µm. **B**. A distortion map of chromatic aberration across the entire FOV (83 µm×83 µm) of the objective lens used for all imaging experiments. The arrows indicate displacement vectors corresponding to chromatic shift direction from *magenta* (561 nm) channel to *green* (488 nm) channel directions. The lengths of the vectors are exaggerated (by multiplying each displacement vector by $50/r_{max}$, where r_{max} = longest displacement vector) for clearer visual representation (34). **C**. Distribution of Euclidean distances between centroids of TetraSpeck beads in two channels (d_{MG}) in images 'uncorrected' and 'corrected' for chromatic aberration. **D**. Distribution of Euclidean distances between the centroids of sub-diffraction spots in *magenta* and *green* channels for several dually labelled particles. The *magenta* and *green* colored '+' signs adjoining the schematics are used to denote whether the centroids in corresponding channels are likely to overlap or not. Data was binned into 20 nm intervals for all distributions. All error values denote standard error.

Finally, we sought to test a dually labeled system which best represented the fluorescence signal level expected in an actual fusion experiment. We found that the RNA of intact influenza virus particles can be fluorescently labeled by incubating a virus suspension with a buffer containing QuantiFluor, similar to previously described methods for labeling of viral genomes (35, 36). We prepared virus particles having the lipid membrane labeled with Texas Red-DHPE and the RNA labeled with QuantiFluor. Dually labeled virus particles adsorbed to plasma-cleaned glass surface were imaged and a mean d_{MG} value of 26.6±1.0 nm was measured (Figure 5D). We combined all d_{MG} distributions from objects with fully co-localizing magenta and green signals into

cumulative distribution functions and determined the d_{MG} value below which 95% of the distances lie (Figure S11). In the case of dually labeled virus particles, 95% of d_{MG} values were below 58 nm which may be chosen as the limiting value below which two signals may be interpreted as fully overlapping. Therefore, we arbitrarily chose 58 nm as the cut-off value to distinguish between symmetric (<58 nm) and non-symmetric (>58 nm) content distribution obtained in the viral fusion experiments as will be described in the next sections.

To measure the viral content distribution within the fused volume as illustrated in Figure 4A, ideally the viral fusion experiment needs to be carried out in a configuration where the virus and vesicle are placed side-by-side. Initially we attempted to obtain this information by carrying out fusion between virus particles with vesicles tethered to a PLL-PEG coated surface as illustrated in Figure 1B. We obtain a distribution of d_{MG} values ranging roughly between 0-150 nm with a mean of 59.9±2.2 nm (Figure S12A) – a value significantly higher than the corresponding d_{MG} values (<30 nm) obtained for objects where two signals are perfectly overlapping as shown in Figure 5D. The data clearly indicates that many fusion events were characterized by a non-symmetric content distribution which is expected to yield larger d_{MG} values as compared to symmetric content distribution. However, we must also consider that in this fusion configuration, from simple geometric arguments, there will be certain limiting conditions where a symmetric and non-symmetric fusion volume will be indistinguishable. For example, a virus bound near the polar regions of a vesicle (as schematically shown in Figure 1B) will lead to nearly identical d_{MG} values for both symmetric and non-symmetric modes of fusions (Figure S12B). In such situations, the d_{MG} values will be underestimated for non-symmetric fused volumes.

Inspired by a previously described strategy for vesicle tethering (37), we designed an experimental configuration where it is possible to increase the likelihood for viruses to bind close to the equatorial regions of the target vesicles and achieve fusion in a side-by-side configuration. We prepared a supported lipid bilayer (SLB) using the gel-phase (at room temperature) forming lipid DPPC and small fractions of two sets of orthogonal DNA-lipid conjugates (**L-dN$_{24}$1** and **L-dN$_{24}$2**, Figure 6A) (37, 38) that can serve as binding sites for objects (vesicles and viruses) bearing DNA-lipid conjugates with complementary sequences (i.e., **L-dN$_{24}$1′** and **L-dN$_{24}$2′**, respectively). We chose a mole fraction of the DNA-lipid conjugates with respect to DPPC such that there are approximately 4 DNA-lipid conjugates of each type on average within a 100 nm×100 nm region of the SLB. We assumed that some virus particles incorporating a DNA-lipid conjugate will initially dock at pH 7.4 on to vesicles via GD1a receptors, following which they will also tether strongly to the SLB by hybridizing with a nearby complementary DNA sequence. In this way, a vesicle-virus pair can be positioned next to each other on the SLB and, because of the gel nature of the SLB, they will not be free to diffuse, essential for the super-localization measurements described in the following. Also, the gel-phase membranes are expected to be mechanically stiffer than fluid phase membranes and therefore the virions are not expected to fuse to the SLB itself (39). We first tethered target vesicles displaying GD1a to the SLB via DNA-lipid conjugate **L-dN$_{24}$1′** (Figure 6A) and washed away unbound vesicles (Figure S13A). In control conditions where no DNA-lipid conjugate was added to the SLB or the target vesicles or both, no or minimal tethering of vesicles to the SLBs was detected. Next, we added the virus particles pre-incubated with DNA-lipid conjugate **L-dN$_{24}$2′** and allowed them to simultaneously attach to GD1a receptors on the vesicle surface and to the DNA strand on the SLB surface. We noted that attachment of a virus particle next to a vesicle is an inherently low probability event. Only 10 virus particles (internally labeled with QuantiFluor) per 1000 target vesicles were observed to tether to the SLB via DNA-lipid conjugates next to a vesicle when the vesicles lacked GD1a. However, when GD1a

was present on the vesicles, the probability of association increased ~4 times (43 per 1000) (Figure S14).

We measured the d_{MG} within a fusion volume between 100 nm vesicles and viruses and obtained a significantly broader distribution of d_{MG}'s ranging between 0-150 nm and a mean of 68.2±2.4 nm (Figure 6B). This value is significantly larger than that obtained for fusion of virus particles with 100 nm vesicles tethered to PLL-PEG surface (Figure 12A), which suggests that the tethering strategy in Figure 6A indeed increases the probability of side-by-side fusion. To test the consistency of our methodology, we asked whether the range of measured d_{MG} values increases if the size of the fused volume is increased. We carried out fusion between 200 nm vesicles and viruses, and indeed d_{MG} values were spread over larger range (0-250 nm) with a significantly higher mean of 82.4±2.8 nm (Figure S15) as compared to the case with 100 nm vesicles.

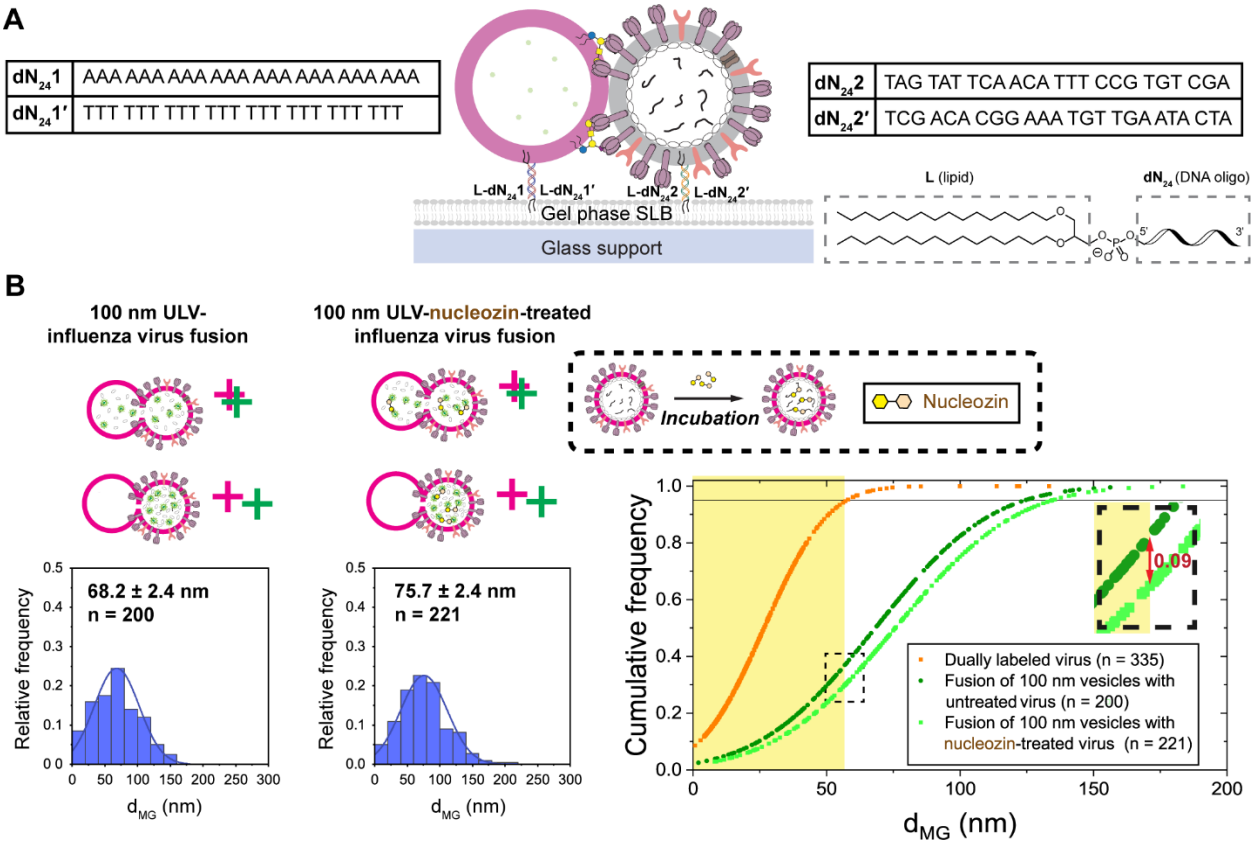

Figure 6. Fusion between virus particles and vesicles in a side-by-side configuration. **A**. Vesicles (Texas Red-DHPE-labeled, encapsulating QuantiFluor and displaying GD1a) and influenza virus particles are sequentially tethered to a gel phase (DPPC) supported lipid bilayer (SLB) via DNA-lipid conjugates (L-dN_{24}'s) in a sidewise fashion. The sense/antisense sequences (5′→3′) of DNA are provided in the tables and the generic structure of a DNA-lipid conjugate is shown. **B**. Distribution of d_{MG}'s for fused volume between 100 nm vesicles and influenza viruses (untreated or treated with nucleozin). The size of nucleozin molecule is exaggerated in the schematic diagram to highlight its effect on aggregation of vRNPs. The *magenta* and *green* colored '+' signs adjoining the schematics are used to denote whether the centroids in corresponding channels are likely to overlap or not. All error values denote standard error. Cumulative distribution function plots of distances between the centroids of membrane and content signals for - dually labeled influenza virus particles; fused volumes between 100 nm vesicles and influenza virus; and fused volumes between 100 nm vesicles and influenza virus pre-treated with nucleozin. The shaded region corresponds to distances less than 58 nm which is the value below which 95% of all the d_{MG}'s measured for dually labeled viruses belong.

Next we sought to test the effect of a drug which is likely to influence the passage of vRNPs through the fusion pore. Nucleozin is a small molecule drug which is known to cause aggregation of vRNPs *in cellulo* or *in vitro* via bridging NPs together (8, 40, 41). Therefore, we hypothesized that influenza virus particles treated with nucleozin will contain aggregated vRNPs which will be less likely to pass through the fusion pores and therefore lead to higher d_{MG} values. Influenza virus particles were incubated with nucleozin and then allowed to co-tether with vesicles to the SLB surface as described above. Interestingly, we measured a broader distribution of d_{MG} values, and a higher mean value of 75.7±2.4 nm (Figure 6B) as compared to the case of fusion of an identical preparation of vesicles with an identical batch of untreated viruses (68.2±2.4 nm). The d_{MG}'s from viral fusion experiments along with those from dually labeled influenza virus (Figure 5D) were plotted into a cumulative distribution function (Figure 6B). Since 95% of the d_{MG}'s for the dually labeled influenza virus fall below 58 nm, we chose this number as a cut-off value for distinguishing between symmetric (<58 nm) and non-symmetric (>58 nm) modes of fusion. In the case of untreated sample, 39% of all d_{MG}'s fell below 58 nm while in case of nucleozin-treated sample, 30% of all d_{MG}'s fell below 58 nm (Figure 6B). The data supports our initial hypothesis that nucleozin causes aggregation of vRNPs and therefore transfers through the fusion pore less efficiently. Given that this analysis is subject to key assumptions such as choice of cut-off value for d_{MG}, we suggest that the results should be interpreted in a semi-quantitative and relative sense rather than an absolute measure. Also, to derive meaningful conclusions, comparison between like systems should be made. Although nucleozin has been described to exert its anti-influenza action by causing nucleoprotein aggregation in the cytoplasm and thereby prevent its nuclear import (42), its effect on the endosomal escape has not been reported so far. Therefore, based on our prediction, it will be interesting to discover whether nucleozin and other nucleoprotein-binding drugs (43–45) can be found to exert inhibitory effects on viral content release in cell-based studies as well.

Conclusion

In summary, we developed a method based on the pseudo-infection model to visualize the transfer and distribution of viral macromolecular contents to target vesicles. Until now, this model has been utilized to characterize the earliest stages of viral infection, such as, binding of virus particles to membrane-bound receptors, and mixing of viral and vesicular lipid compartments and contents. Moreover, from previous content mixing assays based on dequenching of water-soluble dyes, it is not possible to infer whether the viral contents themselves completely mixed within the fused volume. Also, in a previous genome exposure assay (17), the issue of distribution of viral contents within the fused volume was not addressed. Here we show that the utility of pseudo-infection model can be expanded to probe the distribution of viral contents within the fused volume. Whereas in the past the question of viral content distribution has been addressed using advanced structural techniques like cryo-ET, we showed that relatively simpler fluorescence microscopy-based measurements can be used to derive such spatial information.

We foresee that our method of probing viral content transfer to target vesicles using a fluorogenic dye will find many applications in virology and related disciplines. For example, viral infectivity is typically measured using cell culture-based methods which are typically expensive and time-consuming (46). Therefore alternate methods for quantification of viral infectivity which are rapid and do not require cell cultures are highly desirable. Cell-free measurement of viral infectivity may allow assessment of the effects of antiviral therapeutics like neutralizing antibodies (47) or small molecules (48) which block cellular entry or inhibitors of fusion pore formation like IFITM3 (12, 49) in a straightforward manner. Cell-free methods will also be beneficial for

measuring infectivities of BSL-3 agents like highly pathogenic avian influenza (HPAI) A strain H5N1 and SARS-CoV-2 rapidly while generating minimal biohazardous waste, which will facilitate pandemic preparedness research. In our method, detection of a content transfer event implies that a virus particle has functional spike proteins, contains nucleic acid, and forms a fusion pore, all of which are necessary conditions of infectivity. Due to the fluorogenic nature of the RNA-binding dye, detection of fusion events is essentially background-free, so counting of such events (i.e., new fluorescent spots) is straightforward and minimally prone to artifacts and spurious events. Also, our method is suitable for studying the fusion behavior of any enveloped virus given that the viral receptor-ligand pair is known. For instance, influenza viruses that bind to human receptors can be made to fuse with a target vesicle provided it is functionalized with α2,6 sialic acid containing glycolipids. Therefore, it will be interesting to investigate whether counting the number of full fusion events can be directly correlated to viral infectivity obtained from cell-based assays and such efforts are currently underway.

Our incorporation of super-localization microscopy principles into the pseudo-infection model will likely expand the utility of this model to address many general problems in membrane biophysics which deal with the efficiency of transfer of vesicular contents. For example, our method will be useful to interrogate the mechanistic details of agents which are thought to inhibit expansion of fusion pores induced by viral fusion proteins (12, 50). It will also be possible to interrogate whether viral proteins alone are sufficient for fusion pore stabilization and expansion or whether host cellular factors are also responsible (51). In this regard, an improvement in photophysical properties of the RNA-binding dye will allow sequential imaging, and it may be possible to study the evolution of content distribution pattern as a function of time. Finally, we foresee that our method of content distribution assay based on super-localization microscopy can be further adopted for estimating the efficiency of endosomal escape of lipid nanoparticles (LNPs) which is still largely an empirical subject (52, 53). A reliable and straightforward measure of the content distribution between LNPs and target vesicles (mimicking endosome) will likely reflect its endosomal escape behavior and thus facilitate rational design of such nanocarriers.

Materials and Methods

Chemicals and General Considerations. Palmitoyl oleoyl phosphatidylcholine (POPC), dioleoyl phosphatidylethanolamine (DOPE), dipalmitoyl phosphatidylcholine (DPPC), cholesterol, and 16:0 Biotinyl Cap PE were purchased from Avanti Polar Lipids (Alabaster, AL). Texas Red-1,2-dihexadecanoyl-*sn*-glycero-3-phosphoethanolamine (Texas Red-DHPE), Alexa Fluor 488 (succinimidyl ester), and NeutrAvidin were purchased from Thermo Fisher Scientific. Sepharose CL-4B, disialoganglioside GD1a (from bovine brain), and IGEPAL were purchased from Sigma-Aldrich. Chloroform, methanol, HEPES buffer, and buffer salts were obtained from Fisher Scientific and Sigma-Aldrich. Polydimethylsiloxane (PDMS) was obtained from Ellsworth Adhesives (Hayward, CA). Poly(L-lysine)-graft-poly(ethylene glycol) and poly(L-lysine)-graft-poly(ethylene glycol) biotin were purchased from SuSoS (Dübendorf, Switzerland). Nucleozin was purchased from Cayman Chemicals. Proteinase K was purchased from Thermo Fisher Scientific.

Preparation of buffers.The following buffers were used and osmolality values were measured on an Advanced Instruments Micro-Osmometer 3320:

Vesicle buffer: 10 mM Na-phosphate, 90 mM sodium citrate, and 150 mM NaCl (pH 7.4). Osmolality:545 mOsmol/kg.

Fusion buffer: 10 mM Na-phosphate, 90 mM sodium citrate, and 150 mM NaCl (pH 5.1). Osmolality: 510 mOsmol/kg.

Lysis buffer: 100 mM Tris (pH 7.5), 100 mM NaCl, 5 mM $MgCl_2$, 3 mM DTT, 1% (v/v) IGEPAL.

Note on dyes. We communicated with the technical support division of Biotium and confirmed that Oxazole Gold is identical to SYBR Gold available from other suppliers. Biotium also informed us that the stock solution of Thiazole Green (SYBR Green I) has a concentration of ~10 mM. We preferred to prepare vesicles in the absence of any DMSO which may affect membrane properties, so we attempted to remove DMSO from each commercially available dye stock solution by lyophilization and re-dissolved the residue in Milli-Q water. We found that the SYTO family of dyes could not be re-dissolved in this manner and most of the dye remained stuck to the plastic tube walls. In the case of SYTO 12, when an aqueous solution of the dye was made, the yellow color faded within 30 min, suggesting that the compound may be unstable. Only EvaGreen was commercially available as an aqueous solution (25 µM) and it was concentrated to 0.5 mM. Indolizine dye (Table 1, Figure S7) was soluble in water and stored as a 1 mM stock solution. A few simple mathematical calculations were useful as a guide to choose the concentration of a dye in the hydration solution: (i) if the concentration of a molecule in bulk is 100 µM, there are ~30 molecules inside of a 100 nm vesicle (ii) if the concentration of a molecule in bulk is 10 µM, there are ~3 molecules inside of a 100 nm vesicle. See Figure S1 for structures of dyes where available.

Microscopy. Fluorescence images were acquired with a Nikon Ti-U microscope using a 100X oil immersion apochromat TIRF objective (NA = 1.49) (Nikon Instruments, Melville, NY). A Spectra-X LED Light Engine (Lumencor, Beaverton, OR) was used for illumination, and an Andor iXon 897 EMCCD camera (Andor Technologies, Belfast, UK) with 16-bit image settings. Images were captured with Metamorph software version 7.7.11.0 (Molecular Devices, Sunnyvale, CA).

Preparation of DNA-lipid cpnjugates. DNA-lipid conjugates having a general structure as shown in Figure 6A above were synthesized as previously described (38). The DNA-lipid conjugates were dissolved at desired concentration in *vesicle buffer* and stored at -20 °C.

Influenza virus preparation. Influenza A virus (strain X-31, A/Aichi/68, H3N2) grown in the allantoic cavity of SPF eggs was purchased from Charles River Laboratories (Wilmington, MA). The main stock (HA titer: 32768/0.05 mL, EID_{50}: $10^{9.5}$/mL, protein content: 2 mg/mL) was stored as 20 µL aliquots at -80 °C until use. IAV is a Biosafety Level 2 agent and was handled following an approved biosafety protocol at Stanford University. The commercially purchased virus suspension was directly diluted in *vesicle buffer* for use in content transfer experiments. DNA-lipids were incorporated into the IAV envelope by incubating virus sample at 4 °C on ice overnight. Viruses were lysed by incubating a suspension (15-20 µL of commercially available stock) with *lysis buffer* at 37 °C for 1 h. The insoluble debris was removed by centrifugation at 21,130 rcf for 30 min at 4 °C. The supernatant was collected for studying the turn-on behavior of the nucleic acid binding dyes and for TEM imaging of vRNPs (Figure S9). In the experiments where Proteinase K digestion was performed, SDS-PAGE was carried out to confirm that the viral proteins were completely digested.

Vesicle preparation. A lipid mixture composed of POPC:DOPE:Cholesterol:GD1a:Biotin-DPPE:TR-DHPE by molar ratio of 37.4:20:40:2:0.5:0.1 dissolved in organic solvents (chloroform and methanol) was taken in a glass vial. The solvents were removed under a flow of argon gas, and the film was dried under house vacuum for at least 12 h. The hydration solution containing a nucleic acid-binding dye is added to the vial and the film is hydrated by vortexing. The dispersion is transferred to a 0.6 mL tube and then freeze-thawed 5 times. The dispersion was next extruded through 100 nm or 200 nm polycarbonate filters using a mini extruder device (Avanti Polar Lipids) at least 31 times. The vesicles were purified on a small size-exclusion column packed with Sepharose CL-4B gel (0.8-1 mL wet volume). Eluent was collected in small fractions (70-90 µL)

in 0.2 mL tubes. The fractions containing vesicles were identified from Texas Red-DHPE fluorescence by checking the tubes under UV lamp. Vesicle suspensions were stored at 4 °C and typically used within 2 months. We found that vesicles encapsulating QuantiFluor were stable for over 1 year when stored at 4 °C and can be used successfully for the content transfer experiments. We measured the size distribution and polydispersity of the vesicles using dynamic light scattering using a NanoBrook Omni particle size and zeta potential analyzer (Brookhaven Instruments. For typical vesicle preparations, we measured effective diameters (d_{eff}) of 124.8±2.9 nm (polydispersity = 0.061) and 160.0±3.4 nm (polydispersity = 0.274) for vesicles generated by extrusion through 100 nm and 200 nm membrane filters respectively (Figure S2A). For simplicity, we refer to the above two kinds of vesicles as 100 nm and 200 nm vesicles or unilamellar vesicles (ULVs). The 100 nm vesicles were imaged by cryo-TEM to check for unilamellarity (Figure S2B). Most vesicles were found to be unilamellar with some showing multi-compartment (vesicle-in-vesicle) architecture.

Characterization of QuantiFluor. QuantiFluor® (Promega) is a commercially available dye whose structure and concentration are currently proprietary. We carried out a few characterizations of the dye to roughly estimate the concentration. 500 µL of deep orange colored DMSO solution obtained from Promega was mixed with 5 mL of Milli-Q water, lyophilized, and the measured mass of the orange residue was approximately 0.30 mg. This residue was dissolved in 500 µL Milli-Q water, aliquoted into smaller volumes and stored at -20 °C. The aqueous solution is stable at room temperature for several weeks when kept in dark. The turn-on properties of the dye with RNA remained unchanged through the lyophilization/re-dissolving process. We found that the residue could be re-dissolved in Milli-Q water at concentrations up to 10 times that of the original stock. Additionally, we found that the residue was soluble in methanol, ethanol, and chloroform. However, the dye degraded (color faded and turned yellowish) within a week when a $CDCl_3$ solution of the dye was accidentally left in an NMR tube at room temperature. A UV-Vis spectrum of the dye in Milli-Q water revealed an absorption maximum at 483 nm (Figure S4A). The dye solution was run through HPLC (Figure S4B), and a single peak was identified. Mass spectra of the aqueous solution of the dye were taken and a strong peak at m/z = 291.7 and a weaker peak at m/z = 582.2 were detected (Figure S4C). We assign the peak at m/z = 582.2 to be from $[M^+]$ species and the peak at m/z = 291.7 to be from $[M+H^+]$ species. We assume that there is at least one counter-anion permanently associated with the molecule and the molecular weight may range between approximately 620-660 Da. Given that 0.3 mg of dye residue was present in 0.5 mL solution, we estimate that the concentration of the stock solution of the dye is approximately 0.9-0.95 mM.

Content transfer assay (Figure 2). *Experimental setup*. In a freshly prepared microfluidic flow cell (Figure S3), the channels (glass surfaces) are passivated with PLL-PEG/PLL-biotin-PEG. The vesicles encapsulating QuantiFluor (or another nucleic acid-binding dye) are tethered with the passivated surface via NeutrAvidin. Excess vesicles are removed by rinsing the channel with *vesicle buffer.* Following this, virus particles are added to the flow cell and allowed to bind to the vesicles for ~10 min. Unbound virus particles are removed by rinsing the channel with *vesicle buffer*. pH was dropped by flowing in *fusion buffer* while a continuous video stream was acquired for 1200 frames at 3.47 frames per second. The wait time between lowering of pH and appearance of a bright spot (corresponding to a fusion event) were calculated using custom-written MATLAB scripts (details below). The wait times are plotted into cumulative distribution functions (CDF). At neutral pH (7.4) or at slightly acidic pH (6.4), we did not observe any fluorescence turn on events.

Methodology for analysis of content transfer kinetics. In our methodology for analyzing video data, we employ a multi-faceted approach that primarily revolves around detecting and quantifying pixel intensity variations over time. Initially, the video frames are extracted from .tif files and subjected to preprocessing. This preprocessing involves using a 9×9 averaging filter to smooth pixel values, which significantly enhances the accuracy of our subsequent analyses. This step plays a crucial role in noise reduction, contributing to the improved fidelity of event detection. To further enhance the accuracy of our analysis, we exclude the 3 layers of pixels very close to the edges of the images, as any event occurring there may not be fully captured. Following the initial smoothing step, we implement a multi-threshold strategy to identify substantial changes in pixel intensity across frames. These changes serve as indicators of events of interest. To further refine our data, we incorporate various filtering techniques. This includes the removal of redundant and adjacent pixel events to ensure the independence of detected events. Additionally, we apply a low-pass filter to smooth the signal, facilitating the identification of more subtle changes in intensity. This will be used later with the MATLAB function "findpeaks." By utilizing this function, we can determine the location of peak maxima, their prominence, and their width. Peaks that exceed certain arbitrarily defined thresholds in terms of width and height are considered as fusion events. Once the events are detected, we calculate a cumulative distribution function (CDF) of the wait times. The MATLAB codes are available at the following link: https://github.com/boxerlab/Content-Transfer.

Super-localization experiments (Figures 4, 5, 6). *Preparation of gel phase supported lipid bilayer surface*: A film is created by evaporating a 20 µL of 5 mg/mL solution of DPPC in chloroform in a glass vial. The film is suspended by incubation with 200 µL *vesicle buffer* at 60 °C followed by vortexing. The multilamellar dispersion is extruded through 50 nm polycarbonate filter while keeping the extrusion block on a hot plate (65 °C). 20 µL of the extruded vesicles are taken and DNA-lipid conjugates (**L-dN$_{24}$1** and **L-dN$_{24}$2**) are added as shown in Figure 6A. The solution is kept at 65 °C for 30 min. A flow cell is freshly prepared by plasma cleaning and PDMS bonding and 10 µL of the warm DPPC SUVs incorporating two kinds of DNA-lipids is immediately added to the channels and the flow cell is left at room temperature for ~10 min. A mole fraction of the DNA-lipid conjugates is chosen with respect to DPPC such that there are approximately 4 DNA-lipid conjugates of each kind on average within a 100 nm×100 nm region of the SLB. After this, the channels are rinsed with 2 mL *vesicle buffer*. After this, vesicles displaying appropriate complementary DNA-lipid conjugates are added to the flow cell and allowed to bind for ~10 min. The concentration of vesicles is such that there are approximately 500-600 vesicles per FOV and well-separated from one another. It is notable that in absence of the DNA-lipid conjugates in either or both the SLB or vesicles, no binding of vesicles are observed. In order to test whether the DPPC SLBs have any major defects (micrometer-sized cracks, holes, etc), they were incubated with Texas Red-labeled bovine serum albumin (TR-BSA, Invitrogen). If defects were present, TR-BSA bound to the exposed glass surface at the defect sites and the corresponding fluorescence patterns could be imaged by microscope (Figure S13B). We thoroughly optimized the preparation technique such that we could consistently produce gel phase SLBs free of major defects.

Virus-vesicle fusion and Imaging: After tethering the vesicles and then the viruses according to the scheme outlined in Figure 6A, images were taken in 561 nm (*magenta*) and 488 nm (*green*) channels at various contiguous non-overlapping locations of the imaging slide. No spots were detected in the green channel images. The pH was dropped by flowing in *fusion buffer*. After waiting for 30 min, two channel images were taken at the same positions as previous. In the green (QuantiFluor-RNA) channel, new fluorescent spots could be seen overlapping with magenta (membrane) spots corresponding to each fusion event. The explanation for waiting for 30 min is

that in previous cryo-ET studies, 30 min was arbitrarily chosen as a time interval which is long enough that the fusion structures reached their final morphologies (11, 28, 54). In case of nucleozin experiments, the virus particles labeled with DNA-lipid conjugate were incubated in *vesicle buffer* containing 100 µM nucleozin for 1 h at room temperature.

Chromatic aberration correction: Chromatic aberration correction was carried out using the FIJI plugin Detection of Molecules (DoM) version 1.2.4 according to the instructions provided by the developer: https://github.com/UU-cellbiology/DoM_Utrecht/wiki/Chromatic-correction. Multiply labeled TetraSpeck beads (Thermo Fisher) were used to carry out channel registration. 1 µL of the commercially available dispersion of 100 nm beads were diluted to 100 µL with Milli-Q water and put on bath sonication for 1 h. A fresh microfluidic flow cell (Figure S3) was prepared and functionalized with PLL-PEG. 10 µL of the bead dispersion was added and allowed to adsorb for >10 min. The excess beads were rinsed away. Image stacks were taken consecutively in 488 nm (*green*) and 561 nm (*magenta*) channels with exposure and illumination settings such that pixel intensity values of ~10^4 (maximum possible pixel value for a 16 bit image is 65535) were obtained at the center of a particle. Next, the chromatic calibration table containing the displacement vectors across the FOV was calculated. This table was used to correct the images taken in the magenta channel. When we calculated the distances between magenta-green centroid pairs (d_{MG}) of bead signals using ThunderSTORM plugin, we obtained a mean registration error of 8.9±0.4 nm for the whole FOV after chromatic aberration correction. In comparison, the mean registration error without chromatic aberration correction was 76.1±1.4 nm for the whole FOV.

ThunderSTORM analysis: The FIJI plugin ThunderSTORM (Version 1.3) (33) was used to super-localize the signals from individual diffraction limited particles (fluorescent beads, vesicles, or vesicle-virus fusion volumes). A B-Spline wavelet filter (order = 3, scale = 2.0) was used to filter the images. A local maximum algorithm was used to approximate the localization of particles with 2×std peak intensity threshold (2.0*std(Wave.F1)) and 8-neighborhood connectivity. The point spread function was fitted by a weighted least squares method using a 7-pixel fitting radius and initial sigma of 1.6 pixel. Super-localized coordinates were filtered on the basis of pre-defined "sigma" and "uncertainty" values which were kept constant for all comparative analyses to deduce meaningful comparisons between d_{MG} distributions. The super-localized centroids of particles were corrected for chromatic aberration using DoM plugin wherever applicable. Euclidean distance between two super-localized points in magenta (x_M, y_M) and green channels (x_G, y_G) is defined as $d_{MG} = \sqrt{(y_M - y_G)^2 + (x_M - x_G)^2}$ and they were calculated using the "Colocalization" menu.

Supporting Information

The Supporting Information file contains supplementary figures S1-S15 and supplementary references.

Author Contributions

A.B. and S.G.B conceived the project. A.B. designed and performed the experiments and analyzed the data. N.B. wrote the MATLAB code and analyzed the data for content transfer kinetic analysis. A.B. wrote the manuscript with inputs from S.G.B.

Competing Interest Statement

The authors declare no competing interests.

Acknowledgements

This work was supported in part by NIH Grant GM118044 (to S.G.B.). Electron microscopy imaging carried out at the Cell Sciences Imaging Facility (CSIF) at Stanford University was supported, in part, by ARRA Award Number 1S10RR026780-01 from the National Center for Research Resources (NCRR). We thank Promega for generously providing a sample of QuantiFluor for preliminary studies. We thank Rohini Datta for providing SYBR Gold. We thank Dr Frank R Moss III (SLAC National Accelerator Laboratory) for carrying out cryo-TEM imaging of vesicles. We thank Drs. Katherine N. Liu, Srijit Mukherjee, Robert J. Rawle (Williamson College), and Anish Raj Roy (W.E. Moerner Lab), for helpful discussions during manuscript preparation. We thank the Moerner lab for generously providing 0.1 µm TetraSpeck™ microsphere beads for chromatic calibration, and Professor Chao Zhang (University of Southern California) for generously providing the indolizine dye.

References

1. J. M. White, A. E. Ward, L. Odongo, L. K. Tamm, Viral Membrane Fusion: A Dance Between Proteins and Lipids. *Annu. Rev. Virol.* **10**, 139–161 (2023).
2. M. A. Benhaim, K. K. Lee, New biophysical approaches reveal the dynamics and mechanics of type I viral fusion machinery and their interplay with membranes. *Viruses* **12**, 413 (2020).
3. J. Fontana, A. C. Steven, Influenza virus-mediated membrane fusion: Structural insights from electron microscopy. *Arch. Biochem. Biophys.* **581**, 86–97 (2015).
4. S. Haldar, Recent Developments in Single-Virus Fusion Assay. *J. Membr. Biol.* **255**, 747–755 (2022).
5. S. Banerjee, S. Maurya, R. Roy, Single-molecule fluorescence imaging: Generating insights into molecular interactions in virology. *J. Biosci.* **43**, 519–540 (2018).
6. J. S. Blijleven, S. Boonstra, P. R. Onck, E. van der Giessen, A. M. van Oijen, Mechanisms of influenza viral membrane fusion. *Semin. Cell Dev. Biol.* **60**, 78–88 (2016).
7. E. C. Hutchinson, *et al.*, Conserved and host-specific features of influenza virion architecture. *Nat. Commun.* **5** (2014).
8. R. Coloma, *et al.*, Structural insights into influenza A virus ribonucleoproteins reveal a processive helical track as transcription mechanism. *Nat. Microbiol.* **5**, 727–734 (2020).
9. T. Noda, *et al.*, Architecture of ribonucleoprotein complexes in influenza A virus particles. *Nature* **439**, 490–492 (2006).
10. R. Coloma, *et al.*, The structure of a biologically active influenza virus ribonucleoprotein complex. *PLoS Pathog.* **5**, e1000491 (2009).
11. K. K. Lee, Architecture of a nascent viral fusion pore. *EMBO J.* **29**, 1299–1311 (2010).
12. J. Staring, M. Raaben, T. R. Brummelkamp, Viral escape from endosomes and host detection at a glance. *J. Cell Sci.* **131**, jcs216259 (2018).
13. S. H. C. Park *et al*., Membrane Rigidity-Tunable Fusogenic Nanosensor for High Throughput Detection of IAV. *Adv. Funct. Mater.* **33**, 2214603 (2023).
14. D. L. Floyd, J. R. Ragains, J. J. Skehel, S. C. Harrison, A. M. Van Oijen, Single-particle kinetics of influenza virus membrane fusion. *Proc. Natl. Acad. Sci. U. S. A.* **105**, 15382–15387 (2008).
15. K. N. Liu, S. G. Boxer, Single-virus content-mixing assay reveals cholesterol-enhanced influenza membrane fusion efficiency. *Biophys. J.*, **120**, 4832-4841 (2021).
16. E. R. Webster, K. N. Liu, R. J. Rawle, S. G. Boxer, Modulating the Influenza A Virus-Target Membrane Fusion Interface With Synthetic DNA-Lipid Receptors. *Langmuir* **38**, 2354–2362 (2022).
17. A. M. Villamil Giraldo, S. Mannsverk, P. M. Kasson, Measuring single-virus fusion kinetics using an

assay for nucleic acid exposure. *Biophys. J.* **121**, 4467–4475 (2022).

18. L. D. Hughes, R. J. Rawle, S. G. Boxer, Choose your label wisely: Water-soluble fluorophores often interact with lipid bilayers. *PLoS One* **9**, e87649 (2014).
19. K. N. Liu, S. G. Boxer, Single-virus content-mixing assay reveals cholesterol-enhanced influenza membrane fusion efficiency. *Biophys. J.* **120**, 4832–4841 (2021).
20. Q. Gao, T. Ha, P. Palese, One influenza virus particle packages eight unique viral RNAs as shown by FISH analysis. *Proc. Natl. Acad. Sci. U. S. A.* **109**, 9101–9106 (2012).
21. D. V. Bann, L. J. Parent, Application of live-cell RNA imaging techniques to the study of retroviral RNA trafficking. *Viruses* **4**, 963–979 (2012).
22. S. Mannsverk, A. M. V. Giraldo, P. M. Kasson, Influenza Virus Membrane Fusion Is Promoted by the Endosome-Resident Phospholipid Bis(monoacylglycero)phosphate *J. Phys. Chem. B* **126**, 10445-10451 (2022).
23. X. Luo, *et al.*, Lighting up the Native Viral RNA Genome with a Fluorogenic Probe for the Live-Cell Visualization of Virus Infection. *J. Am. Chem. Soc.* **141**, 5182–5191 (2019).
24. M. J. Kim, *et al.*, Development of Highly Fluorogenic Styrene Probes for Visualizing RNA in living cells. *ACS Chem. Biol*. **18**, 1523-1533 (2023) .
25. G. B. Melikyan, *et al.*, Comparison of transient and successful fusion pores connecting influenza hemagglutinin expressing cells to planar membranes. *J. Gen. Physiol.* **106**, 803–819 (1995).
26. R. M. Markosyan, *et al.*, Induction of Cell-Cell Fusion by Ebola Virus Glycoprotein: Low pH Is Not a Trigger. *PLoS Pathog.* **12**, e1001373 (2016).
27. L. J. Calder, P. B. Rosenthal, Cryomicroscopy provides structural snapshots of influenza virus membrane fusion. *Nat. Struct. Mol. Biol.* **23**, 853–858 (2016).
28. L. Gui, J. L. Ebner, A. Mileant, J. A. Williams, K. K. Lee, Visualization and Sequencing of Membrane Remodeling Leading to Influenza Virus Fusion. *J. Virol.* **90**, 6948–6962 (2016).
29. L. Möckl, W. E. Moerner, Super-resolution Microscopy with Single Molecules in Biology and Beyond-Essentials, Current Trends, and Future Challenges. *J. Am. Chem. Soc.* **142**, 17828–17844 (2020).
30. J. Wang, *et al.*, Multi-color super-resolution imaging to study human coronavirus RNA during cellular infection. *Cell Reports Methods* **2**, 100170 (2022).
31. M. Erdelyi, *et al.*, Correcting chromatic offset in multicolor super-resolution localization microscopy. *Opt. Express* **21**, 10978 (2013).
32. C. Eliscovich, S. M. Shenoy, R. H. Singer, Imaging mRNA and protein interactions within neurons. *Proc. Natl. Acad. Sci. U. S. A.* **114**, E1875–E1884 (2017).
33. M. Ovesný, P. Křížek, J. Borkovec, Z. Švindrych, G. M. Hagen, ThunderSTORM: A comprehensive ImageJ plug-in for PALM and STORM data analysis and super-resolution imaging. *Bioinformatics* **30**, 2389–2390 (2014).
34. Detection and quantification were performed using Detection of Molecules (DoM) plugin v.1.2.4 for ImageJ (https://github.com/UU-cellbiology/DoM_Utrecht).
35. S. L. Liu, *et al.*, High-efficiency dual labeling of influenza virus for single-virus imaging. *Biomaterials* **33**, 7828–7833 (2012).
36. J. L. R. Zamora, H. C. Aguilar, Flow virometry as a tool to study viruses. *Methods* **134**–**135**, 87–97 (2018).
37. B. Van Lengerich, R. J. Rawle, S. G. Boxer, Covalent attachment of lipid vesicles to a fluid-supported bilayer allows observation of DNA-mediated vesicle interactions. *Langmuir* **26**, 8666–8672 (2010).
38. Y.-H. M. Chan, B. van Lengerich, S. G. Boxer, Lipid-anchored DNA mediates vesicle fusion as observed by lipid and content mixing. *Biointerphases* **3**, FA17–FA21 (2008).
39. K. Norling, *et al.*, Dissimilar Deformation of Fluid- and Gel-Phase Liposomes upon Multivalent Interaction with Cell Membrane Mimics Revealed Using Dual-Wavelength Surface Plasmon

Resonance. *Langmuir* **38**, 2550–2560 (2022).

40. R. Y. Kao, *et al.*, Identification of influenza A nucleoprotein as an antiviral target. *Nat. Biotechnol.* **28**, 600–605 (2010).
41. B. Pang, *et al.*, Structural characterization of H1N1 nucleoprotein-nucleozin binding sites. *Sci. Rep.* **6**, 29684 (2016).
42. M. J. Amorim, R. Y. Kao, P. Digard, Nucleozin Targets Cytoplasmic Trafficking of Viral Ribonucleoprotein-Rab11 Complexes in Influenza A Virus Infection. *J. Virol.* **87**, 4694–4703 (2013).
43. S. W. Gerritz, *et al.*, Inhibition of influenza virus replication via small molecules that induce the formation of higher-order nucleoprotein oligomers. *Proc. Natl. Acad. Sci. U. S. A.* **108**, 15366–15371 (2011).
44. F. Yang, *et al.*, Discovery of a Novel Specific Inhibitor Targeting Influenza A Virus Nucleoprotein with Pleiotropic Inhibitory Effects on Various Steps of the Viral Life Cycle. *J. Virol.* **95**, e01432 (2021).
45. E. Correa-Padilla, *et al.*, Modifications in the piperazine ring of nucleozin affect anti-influenza activity. *PLoS One* **18**, e0277073 (2023).
46. R. McCracken, *et al.*, Rapid In-Process Measurement of Live Virus Vaccine Potency Using Laser Force Cytology: Paving the Way for Rapid Vaccine Development. *Vaccines* **10**, 1589 (2022).
47. C. I. Paules, *et al.*, The hemagglutinin A stem antibody MEDI8852 prevents and controls disease and limits transmission of pandemic influenza viruses. *J. Infect. Dis.* **216**, 356–365 (2017).
48. Y. Yao, *et al.*, An influenza A hemagglutinin small-molecule fusion inhibitor identified by a new high-throughput fluorescence polarization screen. *Proc. Natl. Acad. Sci. U. S. A.* **117**, 18431–18438 (2020).
49. C. C. Bailey, G. Zhong, I. C. Huang, M. Farzan, IFITM-family proteins: The cell's first line of antiviral defense. *Annu. Rev. Virol.* **1**, 261–283 (2014).
50. M. Ciechonska, R. Duncan, Lysophosphatidylcholine Reversibly Arrests Pore Expansion during Syncytium Formation Mediated by Diverse Viral Fusogens. *J. Virol.* **88**, 6528–6531 (2014).
51. G. B. Melikyan, Common principles and intermediates of viral protein-mediated fusion: The HIV-1 paradigm. *Retrovirology* **5**, 111 (2008).
52. M. Schlich, *et al.*, Cytosolic delivery of nucleic acids: The case of ionizable lipid nanoparticles. *Bioeng. Transl. Med.* **6**, e10213 (2021).
53. S. F. Dowdy, Endosomal escape of RNA therapeutics: How do we solve this rate-limiting problem? *Rna* **29**, 396–401 (2023).
54. P. Chlanda, *et al.*, The hemifusion structure induced by influenza virus haemagglutinin is determined by physical properties of the target membranes. *Nat. Microbiol.* **1**, 16050 (2016).

Supporting Information

A fluorogenic pseudo-infection assay to probe transfer and distribution of influenza viral contents to target vesicles

Ahanjit Bhattacharya,[1, 2] Nahal Bagheri,[3] Steven G. Boxer[1, *]

[1]Department of Chemistry, Stanford University, Stanford, CA-94305

[2]Stanford Center for Innovation in Global Health, Stanford University, Stanford, CA-94305

[3]Department of Electrical Engineering, Stanford University, Stanford, CA-94305

*Correspondence to: sboxer@stanford.edu

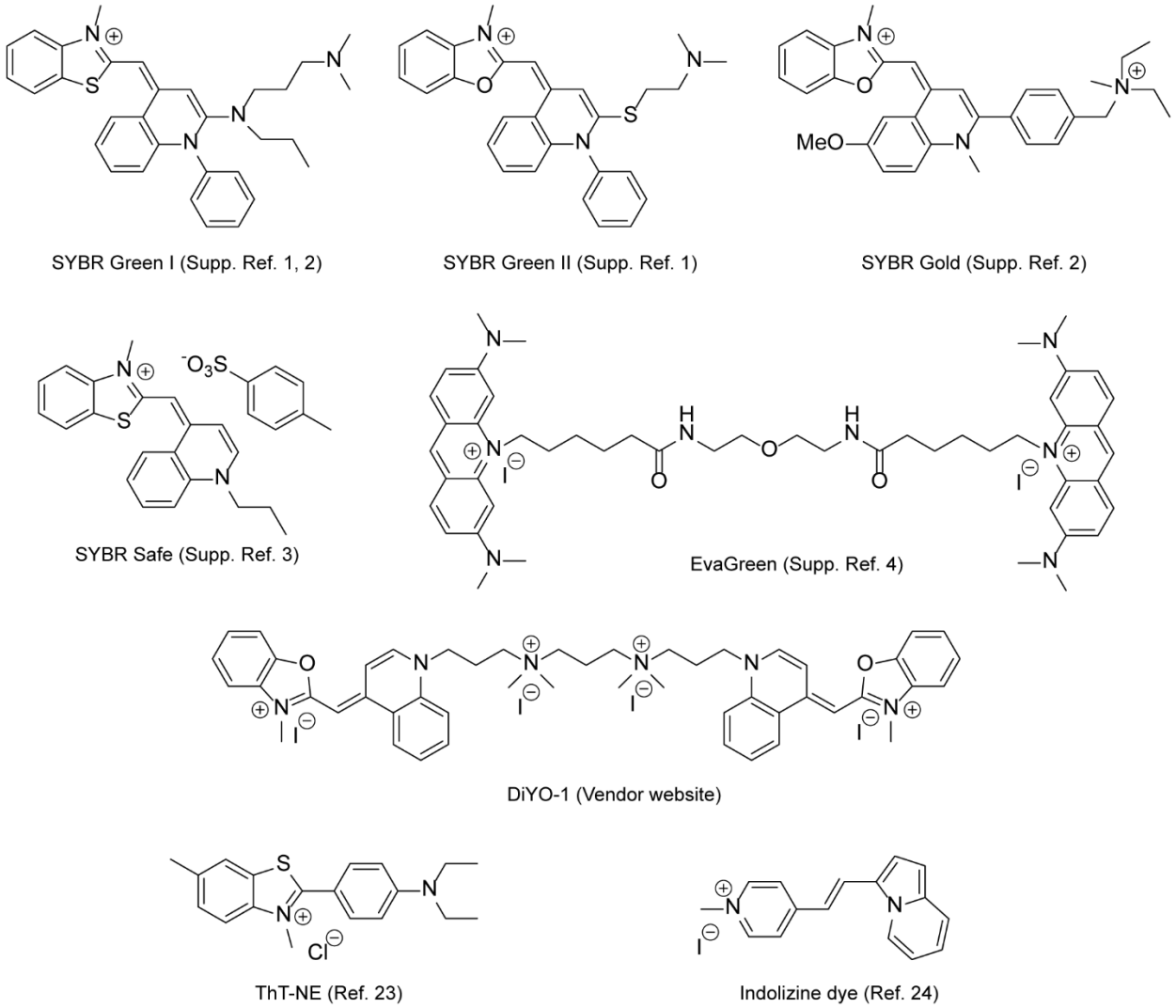

Figure S1. Dyes with known chemical structures used in this work. The structures were taken from indicated references in main text (Ref. 23, 24) or supplementary information (such as for SYBR Green I (1, 2), SYBR Green II (1), SYBR Gold (2), SYBR Safe (3), EvaGreen (4)) or from website of commercial vendor.

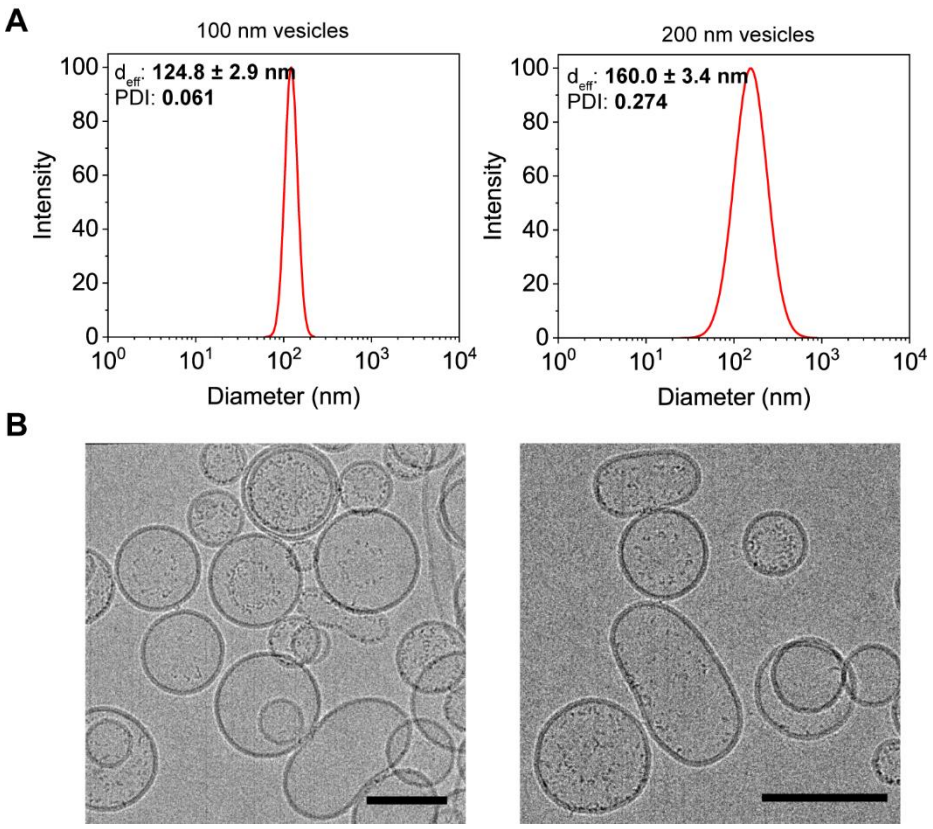

Figure S2. Preparation and characterization of unilamellar vesicles (ULVs) used for viral fusion studies. **A**. Dynamic light scattering (DLS) characterization of vesicles extruded through 100 nm or 200 nm polycarbonate membrane filters and having compositions (37.5:20:40:2:0.5 POPC:DOPE:Cholesterol:GD1a:Biotin-DPPE) representative of what was used in viral fusion experiments. d_{eff}: effective diameter, PDI: polydispersity index. **B**. Cryogenic transmission electron microscopy images of 100 nm vesicles used for viral fusion experiments. Scale bars represent 100 nm.

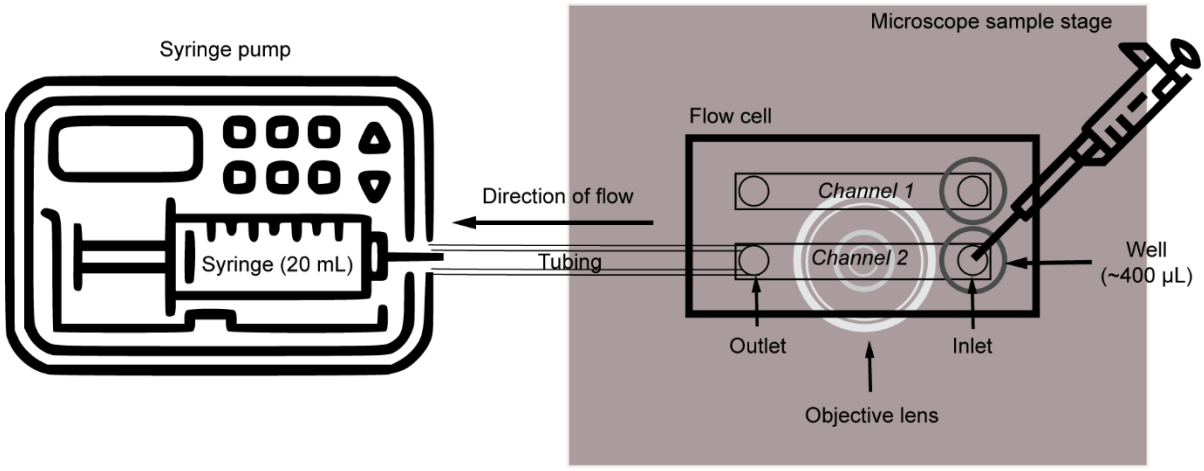

Figure S3. A schematic diagram (*top view*) of the experimental setup used for viral fusion experiments on a microfluidic flow cell. Vesicles and viruses are tethered inside the channels (1 and/or 2).

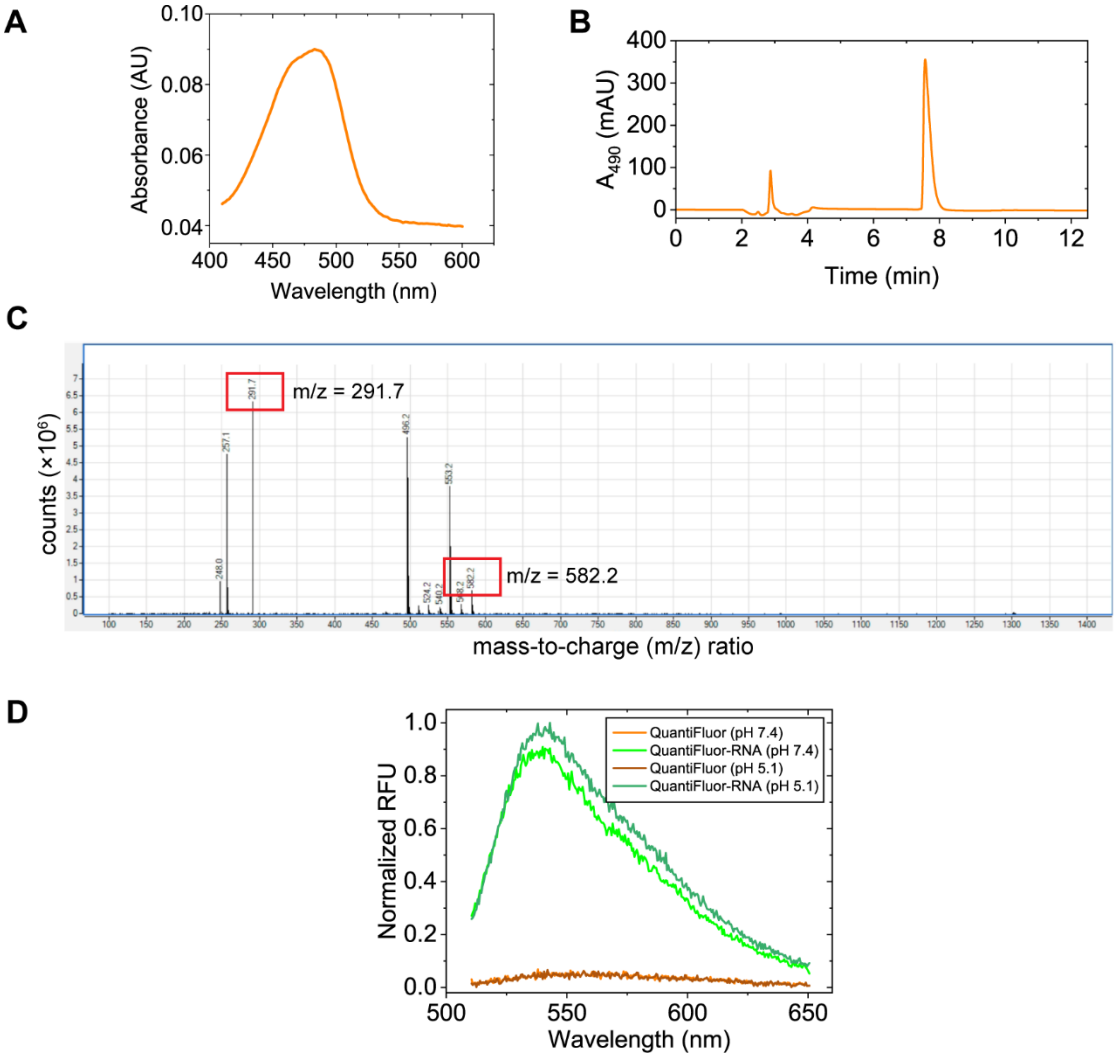

Figure S4. Characterization of QuantiFluor. **A**. Absorption spectrum of a solution of the dye in Milli-Q water. **B**. HPLC chromatogram (490 nm detection, 4 mL/min flow rate) of QuantiFluor dissolved in water injected into a Zorbax C18 semi-quantitative column. The small peak at 3 min is likely not a real analyte peak – rather an artifact often observed at void volume of the column. **C**. ESI-MS analysis of an aqueous solution of QuantiFluor on Agilent Triple Quadrupole instrument (positive ion mode). **D**. QuantiFluor shows negligible fluorescence at pH 7.4 (*vesicle buffer*) or pH 5.1 (*fusion buffer*). The fluorescence increases significantly in the presence of an RNA standard (0.33 ng/µL, Promega) either at pH 7.4 or 5.1. The fluorescence enhancement upon binding to RNA is very similar at these pH values. Excitation wavelength: 492 nm, scan range: 510-650 nm.

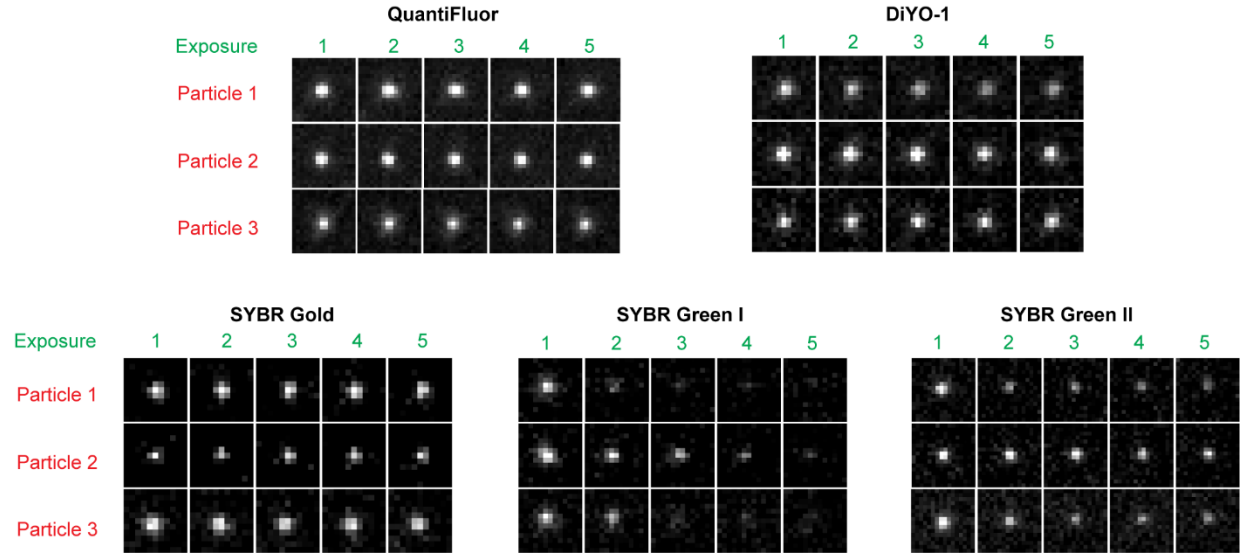

Figure S5. A semi-qualitative comparison of the photostability of various nucleic acid-binding dyes screened for content transfer experiments. Each fluorescent spot (3 representative spots shown for each dye) that represents a fusion event was exposed 5 consecutive times with same illumination intensity and time and images were taken. All images were window-leveled in the identical manner. It can be seen that SYBR Green I has the most inferior apparent photostability as judged from the near-disappearance of the spots by the 4th exposure.

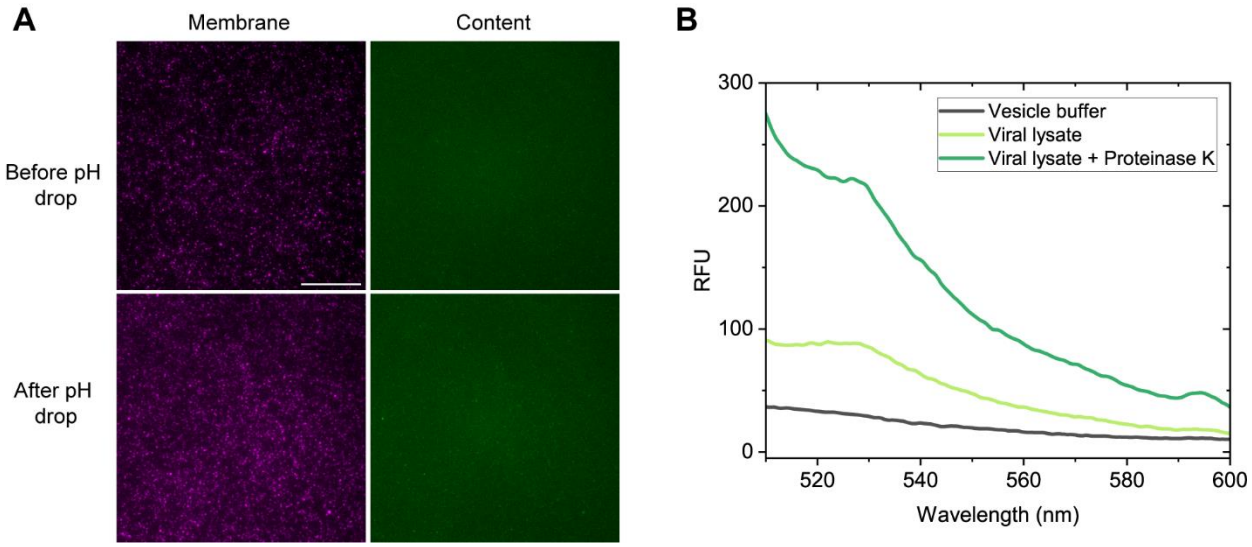

Figure S6. Test of EvaGreen as a content transfer assay dye. **A**. 100 nm vesicles encapsulating EvaGreen were imaged before and after pH drop (7.4 → 5.1) and no "successful" content transfer events were detected as judged from the signals in the "Content" channel. **B**. EvaGreen showed negligible fluorescence in *lysis buffer*. A small increase in fluorescence was observed in presence of lysed virus sample while a significantly larger fluorescence was observed when the lysate was digested with Proteinase K – suggesting that EvaGreen cannot possibly efficiently bind to viral RNA when it is complexed with nucleoproteins.

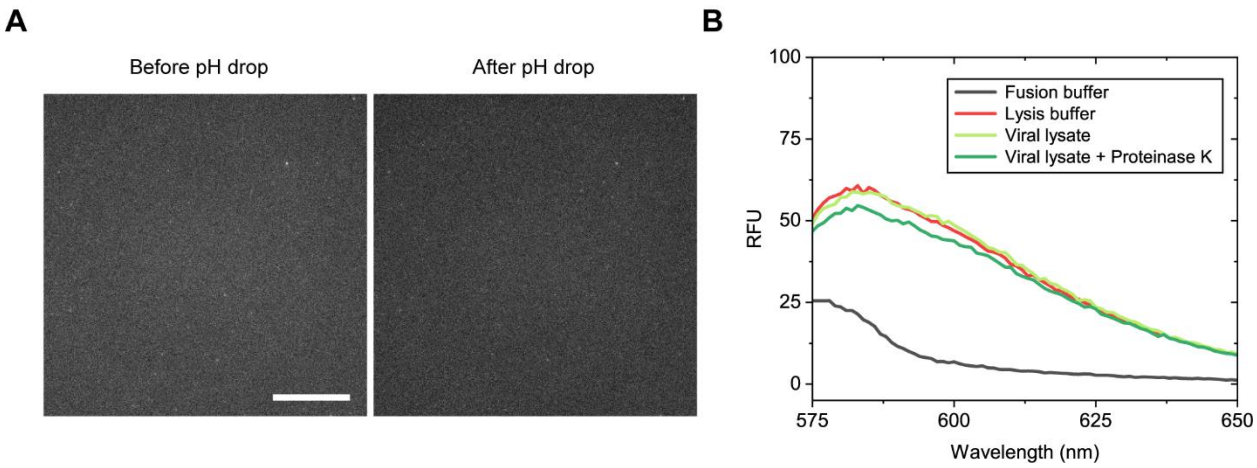

Figure S7. Test of an indolizine dye as a content transfer assay dye. **A**. 100 nm vesicles (37.4:20:40:2:0.5:0.1 POPC: DOPE: Cholesterol: GD1a: Biotin-DPPE: Atto 647N-DMPE) encapsulating the indolizine dye (*E*)-4-(2-(indolizin-3-yl)vinyl)-1-methylpyridinium iodide (5) did not display any fluorescence turn on events after pH drop (7.4 → 5.1) when viruses were added. Scale bar: 20 µm. **B**. When the dye is added to a viral lysate, no significant fluorescence enhancement is detected as compared to the fluorescence of the dye in *lysis buffer* only.

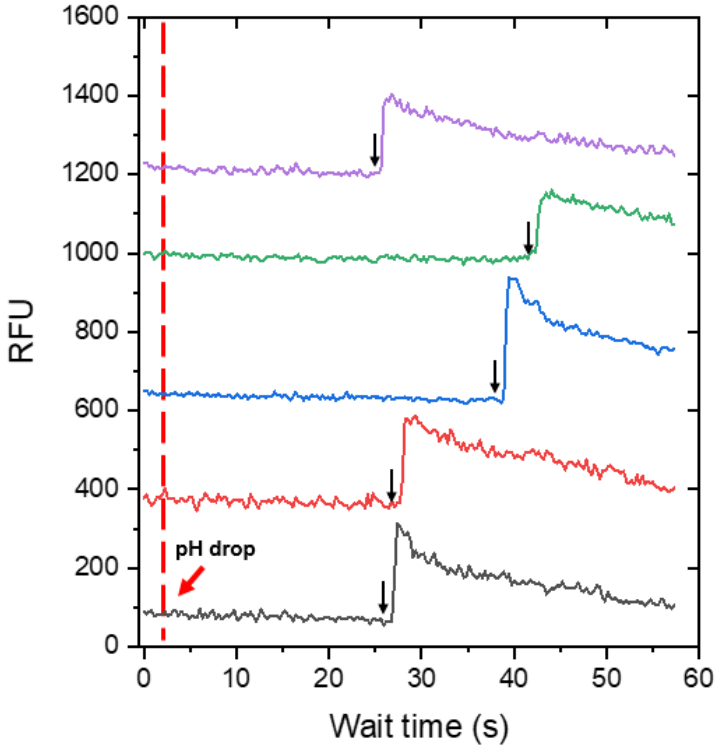

Figure S8. Representative fluorescence intensity traces (from continuous video stream obtained from a single experiment) corresponding to individual fusion events between influenza virus particles and 100 nm vesicles encapsulating QuantiFluor. After a certain wait-time (indicated by black arrows), a sudden spike in the fluorescence signal takes place when the vRNPs bind to QuantiFluor upon fusion. The signal gradually decays due to photobleaching.

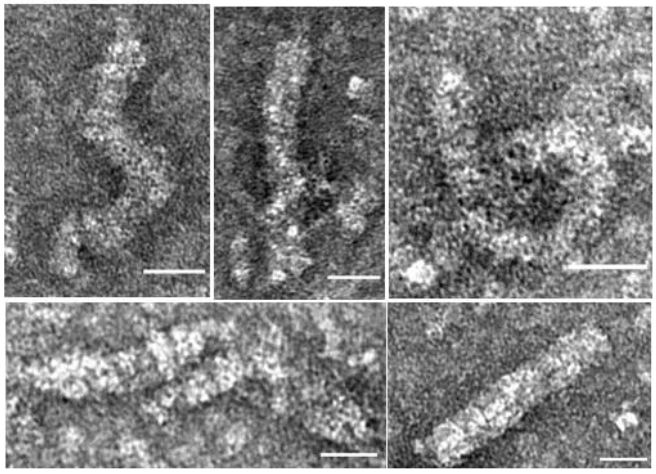

Figure S9. Negative-staining transmission electron microscopy (TEM) images of viral ribonucleoprotein (vRNPs) complexes obtained upon disruption of virus particles with *lysis buffer*. The morphologies of vRNPs are consistent with previous electron microscopy observations (6). All scale bars denote 25 nm. The images illustrate that the vRNPs are well-ordered macromolecular complexes tens of nm in length. Therefore, it is apparent that for vRNPs to freely distribute within the fusion volume, the fusion pore must be several tens of nm in width too.

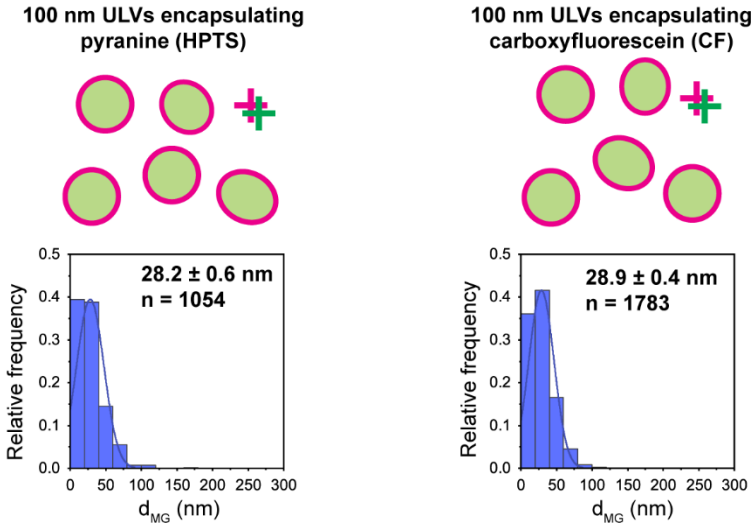

Figure S10. Distribution of Euclidean distances between the centroids of membrane (*magenta*) and content (*green*) dye signals (d_{MG}) for 100 nm unilamellar vesicles (POPC:DOPE: Cholesterol:GD1a:Biotin-DPPE:TR-DHPE 37.4:20:40:2:0.5:0.1 by molar ratio) having membrane labeled with 0.1 mol% Texas Red-DHPE and encapsulating 0.5 mM of the water-soluble dyes pyranine (HPTS) and carboxyfluorescein. The adjoining *magenta* and *green* '+' signs are used to denote whether the centroids in corresponding channels are likely to overlap. The data were binned to 20 nm intervals.

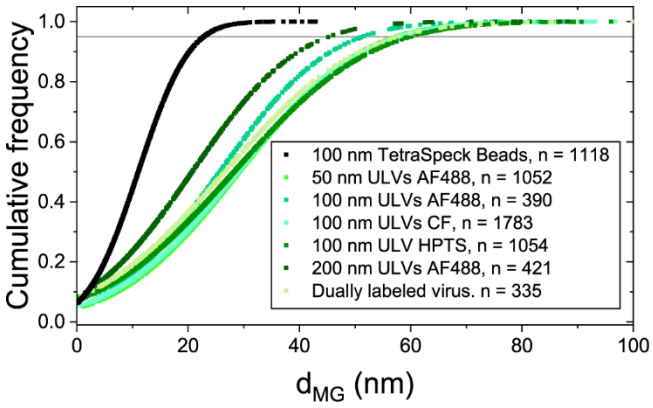

Object	$d_{MG,\ mean}$ (nm)	$d_{MG,\ cut\text{-}off}$ (nm)
100 nm TetraSpeck Beads	11.0 ± 0.2	22.9
50 nm ULVs (AF488)	29.2 ± 0.5	57.5
100 nm ULVs (AF488)	25.7 ± 0.8	51.2
100 nm ULVs (CF)	28.9 ± 0.4	58.0
100 nm ULVs (HPTS)	28.2 ± 0.6	59.9
200 nm ULVs (AF488)	20.7 ± 0.7	45.5
Dually labeled virus	28.6 ± 1.0	57.6

Figure S11. Cumulative distribution functions (CDF) of Euclidean distances between centroids of membrane (*magenta*) and content (*green*) signals (d_{MG}) from objects where the signals fully overlap. The corresponding histograms are shown in Figures 5D and S10. $d_{MG,\ mean}$ represents the mean of the distribution of distances and the errors represent standard error. $d_{MG,\ cut\text{-}off}$ represents the value below which 95% of the d_{MG}'s lie. The row for dually labeled virus is marked in a red box since the corresponding $d_{MG,\ cut\text{-}off}$ value was used to characterize content distribution in viral fusion experiments.

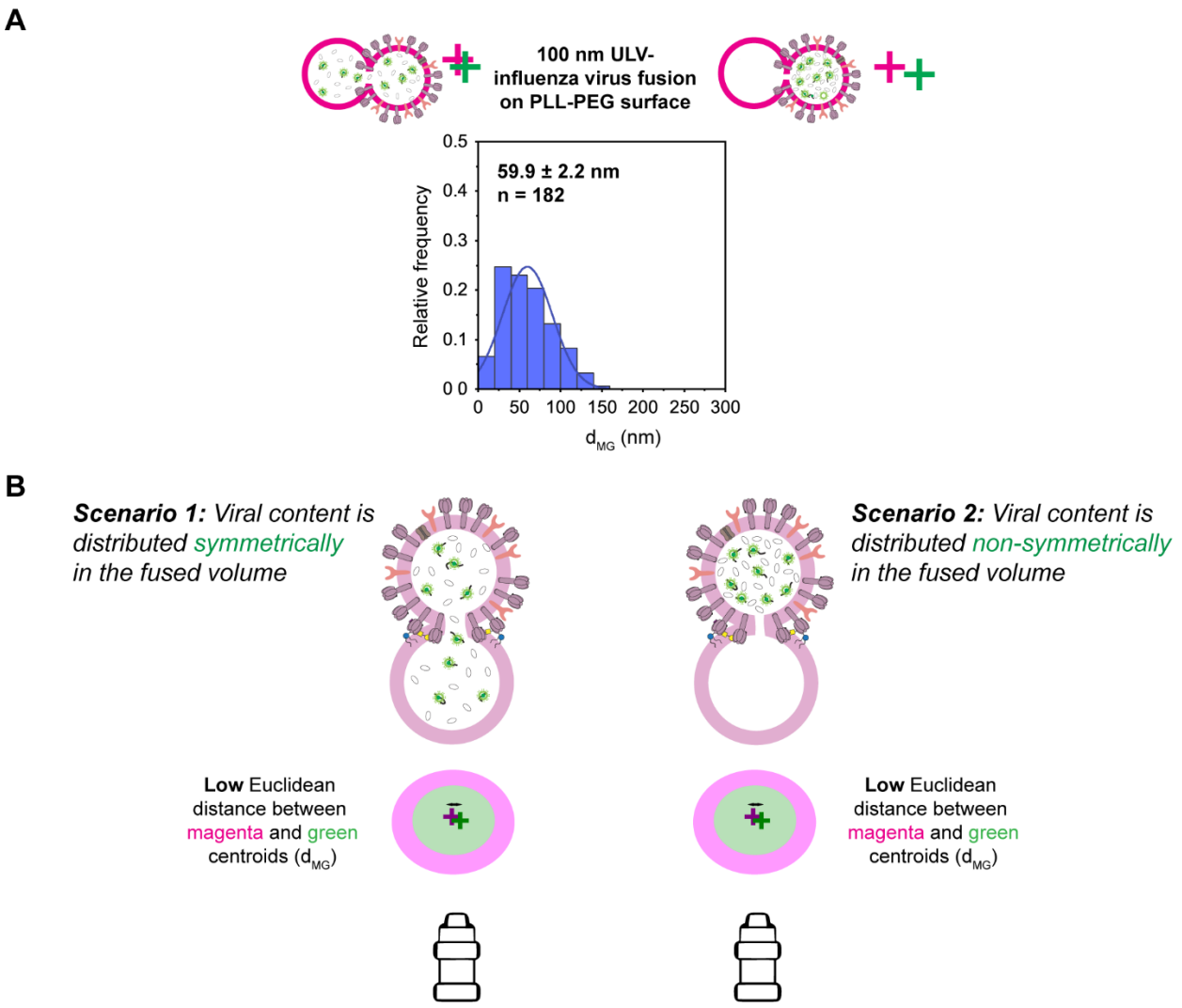

Figure S12. **A**. Distribution of Euclidean distances between the centroids of membrane (*magenta*) and content (*green*) dyes (d_{MG}) corresponding to fusion of 100 nm unilamellar vesicles tethered to PLL-PEG surface with influenza virus as depicted in Figure 1B. **B**. Schematic diagram showing fusion of influenza virus to polar regions of the target vesicles. In such events, no distinction can be made between super-localization microscopy between *Scenario 1*: viral content is distributed non-symmetrically in the fused volume; *Scenario 2*: viral content is distributed non-symmetrically in the fused volume.

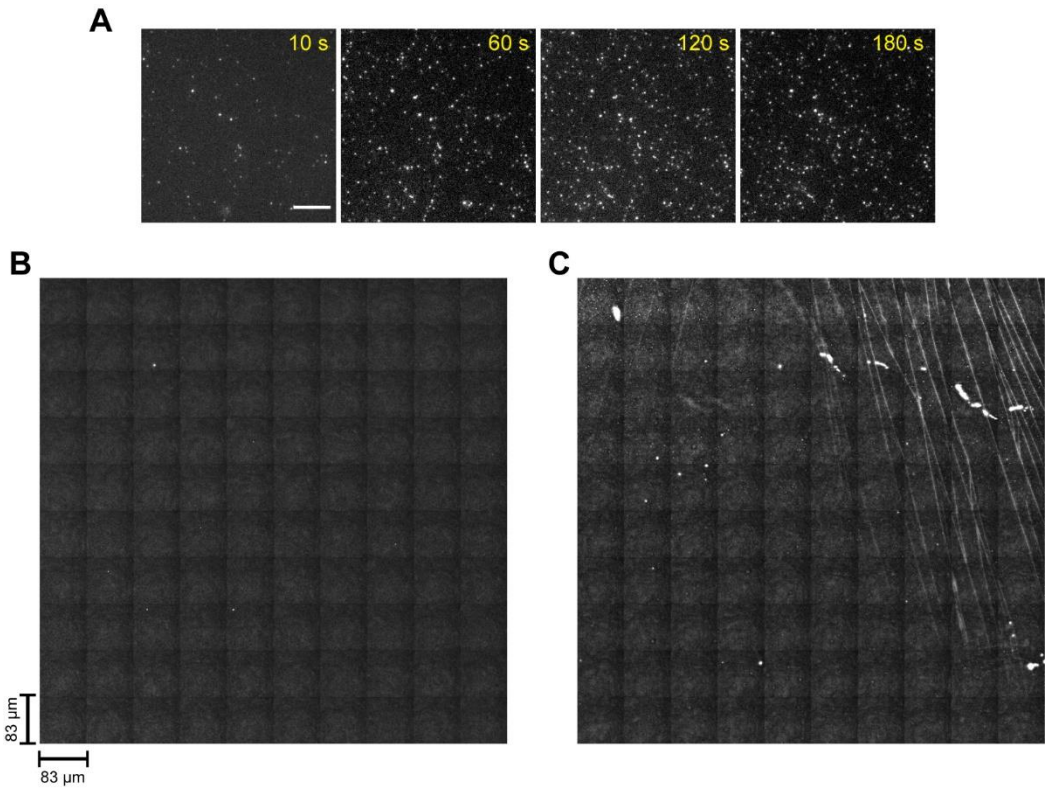

Figure S13. Gel phase supported lipid bilayers (SLB) as a functionalizable surface for carrying out viral fusion experiments. **A**. Time-lapse images of binding of 100 nm vesicles to DPPC SLBs via interaction between complementary DNA-lipid conjugates inserted into the vesicles (**L-dN$_{24}$1'**) and the SLB (**L-dN$_{24}$1**). Scale bar: 20 µm. **B**. A montage of 10×10 contiguous image tiles (each 83 µm×83 µm) of DPPC SLBs treated with TR-BSA showing lack of any micrometer-sized defects. **C**. A montage of 10×10 contiguous image tiles (each 83 µm×83 µm) of DPPC SLBs treated with TR-BSA showing large defects in the form of cracks and voids. It is notable that this SLB was deliberately prepared in a manner that such defects were introduced. In this case, the DPPC SUV solution was added to the plasma cleaned glass slide when it was nearly at room temperature instead of adding it when it is at 65 °C.

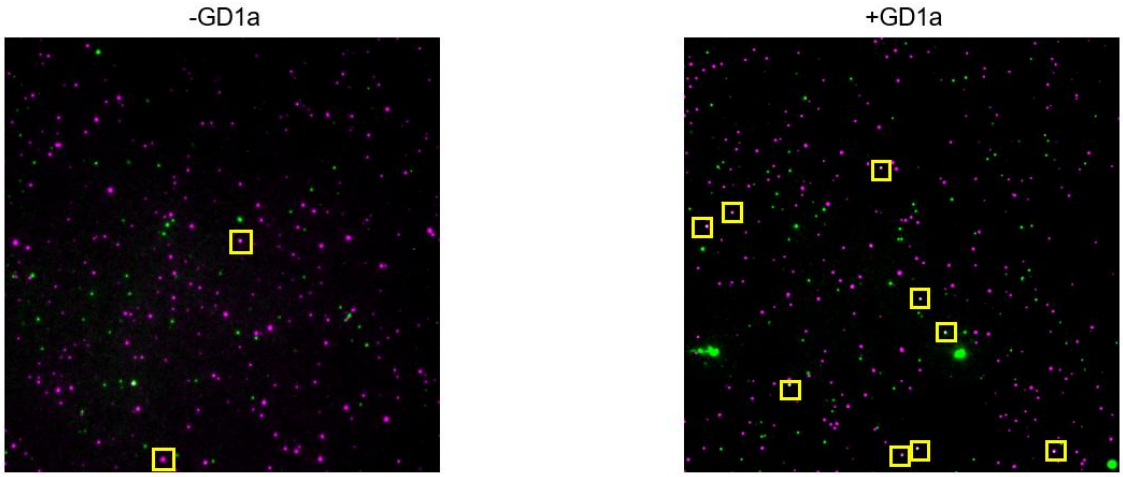

Figure S14. Side-by-side tethering of viruses and vesicles on gel phase (DPPC) supported lipid bilayer (SLB) is a low probability event. 100 nm vesicles (*magenta* spots) lacking (-GD1a) or containing (+GD1a) GD1a in their membranes and influenza virus particles internally labeled with QuantiFluor (*green* spots) were sequentially tethered to DPPC SLBs via two sets of complementary DNA-lipid conjugates as illustrated in Figure 6A. When the vesicles lack any GD1a, chance association of a virus and vesicle is extremely low (10 in 1000). When the vesicles contain GD1a, the chance of association is significantly higher (43 in 1000). The virus particles co-localizing with vesicles are marked in yellow square boxes.

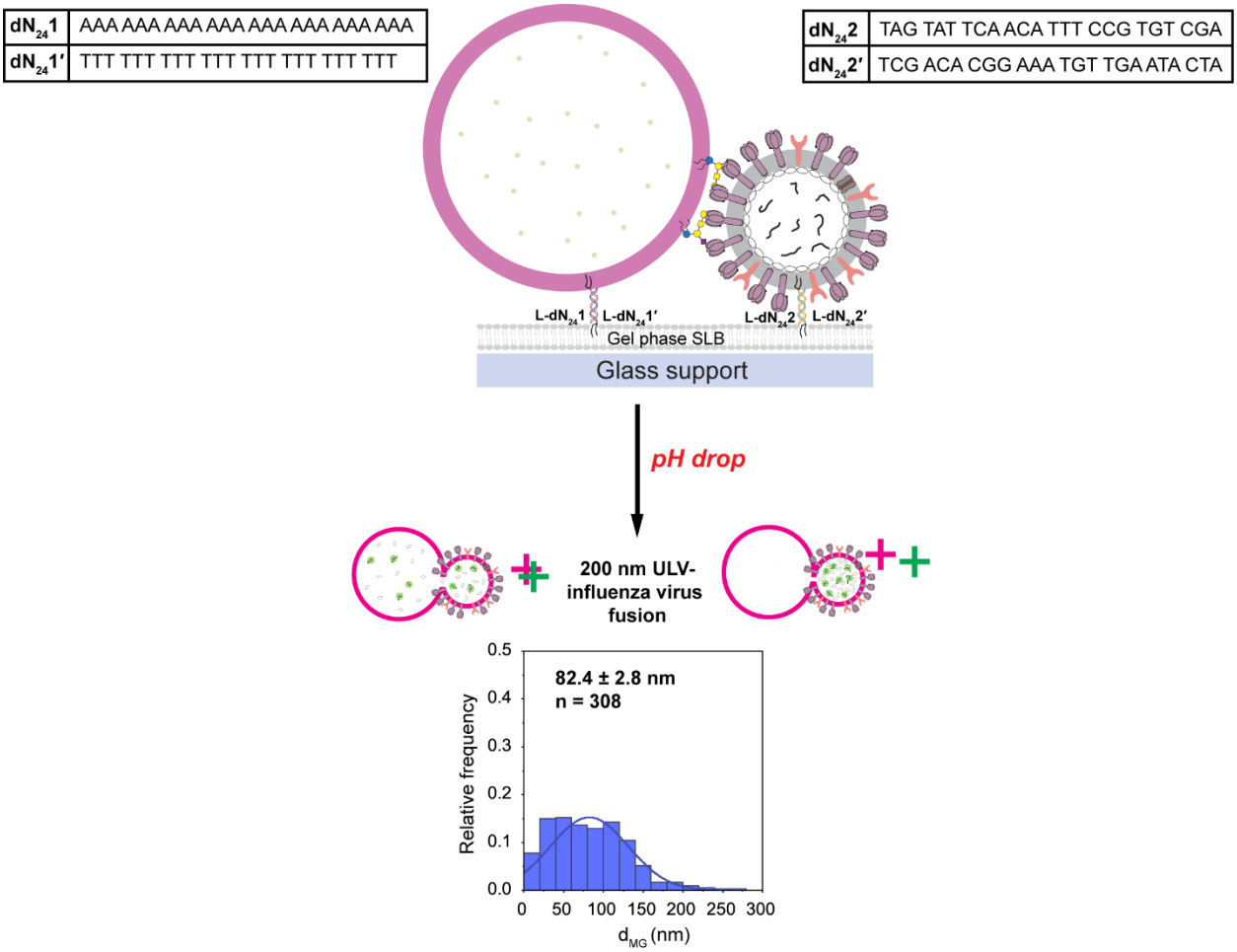

Figure S15. Distribution of Euclidean distances between the centroids of membrane (*magenta*) and content (*green*) dyes (d_{MG}) for 200 nm unilamellar vesicles fused with influenza virus on gel phase SLB surface.

Supplementary References

1. V. K. Saarnio, *et al.*, Development of functionalized SYBR green II related cyanine dyes for viral RNA detection. *Dye. Pigment.* **177** (2020).
2. P. J. Kolbeck, *et al.*, Molecular structure, DNA binding mode, photophysical properties and recommendations for use of SYBR Gold. *Nucleic Acids Res.* **49**, 5143–5158 (2021).
3. W. E. Evenson, L. M. Boden, K. A. Muzikar, D. J. Oleary, ^{1}H and ^{13}C NMR assignments for the cyanine dyes SYBR safe and thiazole orange. *J. Org. Chem.* **77**, 10967–10971 (2012).
4. L. C. T. Shoute, G. R. Loppnow, Characterization of the binding interactions between EvaGreen dye and dsDNA. *Phys. Chem. Chem. Phys.* **20**, 4772–4780 (2018).
5. M. J. Kim, *et al.*, Development of Highly Fluorogenic Styrene Probes for Visualizing RNA in Live Cells. *ACS Chem. Biol.* **18**, 1523–1533 (2023).
6. R. Coloma, *et al.*, Structural insights into influenza A virus ribonucleoproteins reveal a processive helical track as transcription mechanism. *Nat. Microbiol.* **5**, 727–734 (2020).